

Emergence of multiphase condensates from a limited set of chemical building blocks

Fan Chen and William M. Jacobs*

Department of Chemistry, Princeton University, Princeton, NJ 08544, USA

(Dated: December 1, 2023)

Biomolecules composed of a limited set of chemical building blocks can co-localize into distinct, spatially segregated compartments known as biomolecular condensates. Although recent studies of intracellular condensates have shown that coexisting, immiscible condensates can form spontaneously via phase separation, it has remained unclear how coexisting and multiphase condensates assemble from chemical building blocks with limited specificity. Here we establish a connection between the interdependencies among biomolecular interactions and the thermodynamic stability of multiphase condensates. We then introduce an inverse design approach for computing the minimum interaction specificity required to assemble condensates with prescribed molecular compositions in a multicomponent biomolecular mixture. As a proof of principle, we apply our theory to design mixtures of model heteropolymers using a minimal number of distinct monomer types, and we use molecular simulations to verify that our designs produce coexisting condensates with the target molecular compositions. Our theoretical approach explains how multiphase condensates arise in naturally occurring biomolecular mixtures and provides a rational algorithm for engineering complex artificial condensates from simple chemical building blocks.

I. INTRODUCTION

Biomolecules such as proteins and nucleic acids can spontaneously co-localize to form multicomponent condensates via the thermodynamically driven process of phase separation [1–4]. A wide variety of different condensates have been observed in living cells, each of which is associated with a distinct macromolecular composition and the ability to recruit specific client molecules, including enzymes and metabolites [5–7]. Moreover, condensate assembly and disassembly can be regulated by small changes in macromolecular concentrations and the chemical state of the intracellular environment, allowing for dynamic responses of biomolecular co-localization to external stimuli [8–13]. Condensate assembly therefore represents an important mechanism of self-organization in cellular biology, and considerable effort has been devoted to identifying so-called “grammars” that connect the molecular-level properties of specific biomolecules to the condensates that they tend to form [14–18].

Nonetheless, explanations for the observed diversity of condensates, which assemble in a controlled fashion in an extremely heterogeneous intracellular environment, have been elusive. The fundamental paradox stems from the well established biophysical properties of condensate-forming biomolecules. Because key components of condensates, such as intrinsically disordered proteins and many RNAs, are conformationally heterogeneous, these molecules tend to engage in relatively promiscuous, “multivalent” interactions in condensed phases that are fluid in nature [14, 19–22]. Furthermore, many of the molecular grammars that have been developed to describe individual systems, such as arginine/tyrosine compositions of FUS condensates [16] or the aromatic composition of prion-like domain condensates [17], are common to a wide

variety of intracellular biomolecules which do not necessarily co-localize into the same condensates. It has thus been unclear how the *compositional specificity* [23, 24] of multicomponent condensates arises from relatively disordered macromolecules, non-stoichiometric interactions, and existing theories of molecular grammars [25]. Resolving this question is essential to understanding how phase separation can give rise to complex intracellular spatial organization [25].

We propose that this question can be resolved by focusing on the *interaction specificity* of biomolecules. More precisely, we ask what degree of interaction specificity is required to achieve the observed spatial organization in a multicomponent system. Theoretical predictions can then be tested either by quantifying the interaction specificity in a mixture of biomolecules that is observed to phase-separate into distinct coexisting condensates, or by designing “minimal-complexity” biomolecular mixtures—i.e., mixtures that possess the minimum required interaction specificity—that phase-separate into coexisting condensates with prescribed molecular compositions. This approach builds on recent theoretical progress in modeling multicomponent phase separation [25–36], which aims to predict multiphase coexistence using simplified descriptions of biomolecular interactions. However, by focusing on interaction specificity, we can establish a direct connection between multiphase coexistence and the required *physicochemical properties* of biomolecular mixtures.

In this article, we develop a general theoretical description of biomolecular interaction specificity and show how it relates to the thermodynamic stability of coexisting multicomponent condensates. We then introduce an “inverse design” approach [27, 28] for computing the minimum interaction specificity required to form immiscible condensates via phase separation. In addition, our approach establishes a straightforward algorithm for designing minimal-complexity mixtures of biomolecules or syn-

* wjacobs@princeton.edu

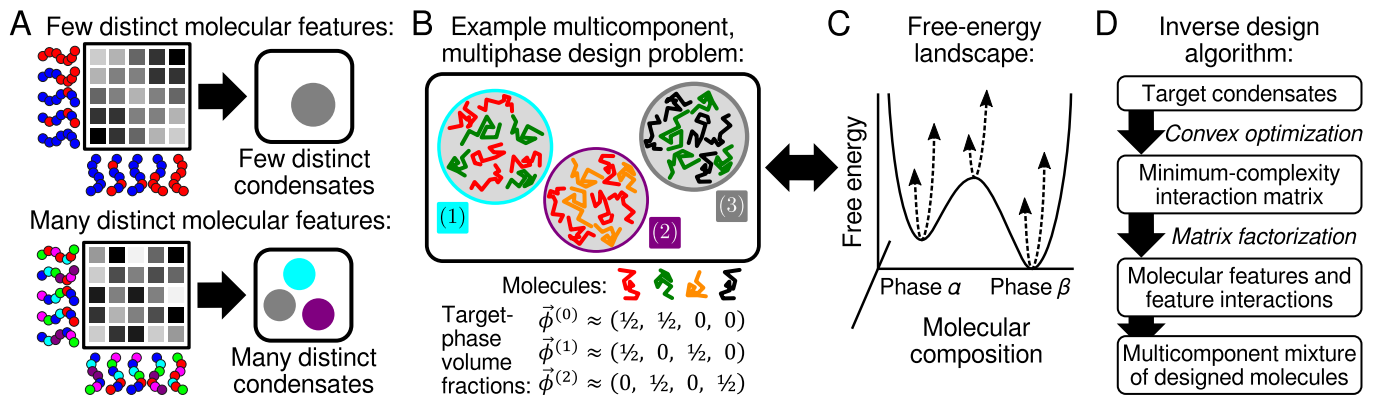


FIG. 1. **Biomolecular interaction interdependencies and inverse design approach.** (A) The interactions between biomolecules in a multicomponent mixture can be described by a pairwise interaction matrix. In a system with few molecular features, such as polymers with a small number of distinct monomer types, the elements of the interaction matrix tend to be interdependent (top). By contrast, in a mixture with many distinct molecular features, the interaction-matrix elements can be independently tuned (bottom). (B) An example multiphase design problem. Here, four molecular species (red, green, gold, and black) phase-separate into three immiscible condensates with prescribed molecular volume fractions $\{\vec{\phi}^{(\alpha)}\}$. (C) A multiphase design problem corresponds to a high-dimensional free-energy landscape, where each target phase (such as the two shown here) specifies a local minimum. (D) To solve the design problem, we first use convex optimization to find the *minimum-complexity* interaction matrix, requiring the smallest number of distinct molecular features, that produces the desired free-energy landscape. We then factorize the minimum-complexity interaction matrix to construct a multicomponent mixture of designed molecules.

thetic macromolecules, subject to system-specific physicochemical constraints, that phase-separate into coexisting phases with prescribed molecular compositions. We demonstrate how this algorithm can be used in practice by designing mixtures of heteropolymers that phase-separate into non-trivial coexisting phases while utilizing a surprisingly small number of distinct monomer types. Finally, we perform molecular dynamics simulations of phase coexistence with these heteropolymer mixtures to validate our theory and inverse design approach. Our results suggest a unifying framework for exploring molecular grammars in biomolecular systems, as well as a practical strategy for engineering complex artificial condensates using experimentally realizable molecules.

II. RESULTS

A. Describing interdependencies among biomolecular interactions

To develop a theoretical description of biomolecular interaction specificity, we adopt a coarse-grained representation of biomolecules in a multicomponent fluid. Specifically, we assume that *pairwise* interactions can be used to describe the net attraction or repulsion between molecular species [25]. This approach implies that the chemical potential μ_i of each macromolecular species $i = 1, \dots, N$ depends linearly on the symmetric pairwise interaction matrix ϵ ,

$$\mu_i(\vec{\phi}) = \mu_{\text{id},i}(\vec{\phi}) + \mu_{\text{v},i}(\vec{\phi}) + \sum_{j=1}^N \epsilon_{ij} \phi_j, \quad (1)$$

where ϕ_i represents the molecular volume fraction (i.e., the concentration times the molecular volume, v_i) of each molecular species i . The first two terms of Eq. (1) account for the ideal, $\mu_{\text{id},i} = v_i^{-1} k_B T \log \phi_i$, and steric, $\mu_{\text{v},i}(\vec{\phi})$, contributions to the chemical potential, which are both independent of ϵ . Eq. (1) provides a coarse-grained description of any homogeneous fluid [37]. However, we make the key approximation that ϵ is independent of $\vec{\phi}$; this means that the net interaction ϵ_{ij} between molecules of types i and j does not depend on the presence of other components in the mixture and is thus the same in all phases. This approximation underlies the Flory–Huggins [38], regular solution [39], and van der Waals models [37], and is consistent with field-theoretic treatments of heteropolymer mixtures [40], with appropriate choices of $\vec{\mu}_v$. Later on, we will use molecular simulations to show that this approximation can yield a remarkably accurate description of multicomponent heteropolymer solutions.

The pairwise interaction matrix provides a systematic way of describing the interdependencies among biomolecular interactions in a multicomponent mixture. In a full-rank interaction matrix, there are $N(N+1)/2$ independent pair interactions. However, because biomolecular interactions are typically governed by a limited set of physicochemical features, it is conceivable that not all pair interactions are independent of one another. For example, in a mixture of molecules that interact via hydrophobic forces alone, there might be only N independent parameters—namely, the hydrophobicity of each molecular species—that determine the interaction matrix. In general, we expect that various modes of interaction, including electrostatic, cation- π , and hydrogen

bonding, among others [14], contribute to the net interactions among biomolecules in a multicomponent mixture.

We formalize this concept of interaction interdependency (Fig. 1A) by factorizing ϵ in terms of a molecular feature matrix, $W \in \mathcal{R}^{N \times r}$, and a feature interaction matrix, $\mathbf{u} \in \mathcal{R}^{r \times r}$ [34],

$$\epsilon = \mathbf{W}\mathbf{u}\mathbf{W}^\top. \quad (2)$$

Here, a “feature” refers to a linearly independent molecular property, which could represent a literal molecular building block such as a nucleotide or an amino acid, or alternatively an emergent property such as a sequence motif or pattern. Each row vector of \mathbf{W} describes the appearance of these features in a particular molecular species, while the matrix \mathbf{u} describes the interactions among all pairs of features. Importantly, the rank r indicates the number of distinct features that are available, and thus controls the number of elements of ϵ that can be independently tuned. An interaction matrix can only be realized in a biomolecular system if r does not exceed the number of available features.

B. Relating interaction interdependencies and biomolecular condensate thermodynamics

Next, to relate the number of available molecular features to the formation of coexisting biomolecular condensates, we take advantage of an *inverse design* approach to condensate thermodynamics [27, 28]. In this approach, we prescribe a set of K target condensed phases (i.e., condensates) with defined molecular compositions (Fig. 1B). Each target condensate $\alpha = 1, \dots, K$ is described by a vector of molecular volume fractions $\vec{\phi}^{(\alpha)}$. For these condensed phases to be thermodynamically stable, each $\vec{\phi}^{(\alpha)}$ must correspond to a local minimum on a free-energy landscape $f(\vec{\phi}) - \vec{\mu}^{(0)} \cdot \vec{\phi}$, where $\mu_i^{(0)}$ is the chemical potential of molecular species i in the dilute phase [37]. From the relationship between the free-energy density f and the chemical potentials, $\mu_i = \partial f / \partial \phi_i$, this stability condition implies that $\mu_i^{(\alpha)} = \mu_i^{(0)}$ for all condensed phases and molecular species. The stability condition also implies that the Hessian of the free-energy density must be positive definite in each condensed phase α , $\partial^2 f / \partial \phi_i \partial \phi_j |_{\vec{\phi}^{(\alpha)}} \succ 0$.

An interaction matrix that solves this inverse design problem establishes a free-energy landscape, following the assumptions of Eq. (1), that is consistent with the prescribed K condensed-phase molecular compositions (Fig. 1C). As such, any mixture with overall macromolecular concentrations within the convex hull of the target-phase and dilute-phase concentrations $\{\vec{\phi}^{(0)}, \vec{\phi}^{(1)}, \dots, \vec{\phi}^{(K)}\}$ can phase-separate to form the prescribed condensed phases [28]. (Whether some or all of these phases form in practice depends on kinetic considerations, such as nucleation dynamics [25, 27], that are not the focus of the present work.) However, the

interaction matrix that solves the design problem is typically not unique. In particular, there may be low-rank interaction matrices, for which $r < N$, that result in—or at least closely approximate—the prescribed condensed-phase molecular compositions. Our goal is to find such low-rank solutions, since they reduce the number of molecular features that are required to achieve the prescribed set of coexisting condensates.

To relate the minimum rank r to a target set of condensed phases $\{\vec{\phi}^{(1)}, \vec{\phi}^{(2)}, \dots, \vec{\phi}^{(K)}\}$, we consider an interaction matrix ϵ that solves this inverse problem. Perturbing ϵ by an error matrix $\Delta\epsilon$ results, to lowest order, in a shift of the condensed-phase compositions (see SI),

$$\Delta\vec{\phi}^{(\alpha)} = -\frac{1}{2} \left(\frac{\partial^2 f}{\partial \phi_i \partial \phi_j} \Big|_{\vec{\phi}^{(\alpha)}} \right)^{-1} \Delta\epsilon \vec{\phi}^{(\alpha)}. \quad (3)$$

Eq. (3) says that the concentrations in the α phase are most sensitive to perturbations in the direction of the eigenvector, $\hat{\nu}_1^{(\alpha)}$, that corresponds to the minimum eigenvalue, $\lambda_1^{(\alpha)}$, of $\partial^2 f / \partial \phi_i \partial \phi_j |_{\vec{\phi}^{(\alpha)}}$. We can therefore relate the Frobenius norm of a random error matrix $\Delta\epsilon$ to the relative change in the molecular compositions of the α phase in this least stable direction, $\eta \equiv 2\Delta\vec{\phi} \cdot \hat{\nu}_1^{(\alpha)} / \|\vec{\phi}^{(\alpha)}\|$ (see SI),

$$\|\Delta\epsilon\|_F \approx \eta \lambda_1^{(\alpha)}. \quad (4)$$

Eq. (4) is useful because it relates the interaction-matrix perturbation to its effect on the phase behavior in the worst-case scenario. Thus, to solve the inverse design problem to within a composition tolerance of η , we must limit deviations of the interaction matrix such that $\|\Delta\epsilon\|_F \lesssim \min_\alpha \eta \lambda_1^{(\alpha)}$.

We can now determine the minimum required interaction specificity by attempting to reduce the number of molecular features, $r \leq N$, used to represent the interaction matrix ϵ . Doing so yields a low-rank approximation, ϵ_r , for the $N \times N$ interaction matrix. Here we apply the Eckart–Young–Mirsky (EYM) theorem [41], which says that $\|\Delta\epsilon\|_F = \|\epsilon_r - \epsilon\|_F$ is minimized by eliminating the $N - r$ smallest singular values of ϵ . Accordingly, the minimum number of molecular features, r , that successfully solves the inverse design problem must satisfy

$$\left[\sum_{k=1}^{N-r} \sigma_k^2 \right]^{1/2} \lesssim \min_\alpha \eta \lambda_1^{(\alpha)}, \quad (5)$$

where $\sigma_1 \leq \sigma_2 \leq \dots \leq \sigma_N$ are the singular values of ϵ . Eq. (5), which relates the singular values of the interaction matrix ϵ to thermodynamic properties of the coexisting condensates, is the central result of our theoretical approach. This equation implies that the inverse design problem can be solved—using the smallest possible number of distinct molecular features—by optimizing ϵ to simultaneously minimize the smallest singular values and maximize the stabilities of the target condensed phases. In this way, our inverse design approach establishes a direct connection between the interdependencies

of pairwise biomolecular interactions and the complexity of the phase-separated condensates that they can form, irrespective of specific details of the molecular features in a particular biomolecular system.

C. Designing low-rank interaction matrices and minimal-complexity biomolecules

In practice, we implement this theory for designing low-rank interaction matrices using convex optimization [42] (Fig. 1D). Then, after the required number of molecular features (i.e., the pairwise interaction matrix rank r) has been determined, we design molecular mixtures by factorizing ϵ , subject to appropriate physicochemical constraints. We discuss each step in turn.

Step 1: Optimization of component-wise interactions. First, we define a convex relaxation of the inverse design problem, such as the example condensate design problem illustrated in Fig. 1B, following the strategy introduced in Refs. [27] and [28]. This step introduces controlled approximations to transform the nonlinear thermodynamic stability and design constraints described in Sec. IIB into a convex optimization problem (see SI for complete details). This convex relaxation is defined by the target condensed-phase volume fractions $\{\bar{\phi}^{(1)}, \bar{\phi}^{(2)}, \dots, \bar{\phi}^{(K)}\}$, the molecular volumes of the N molecular species, and a minimum stability criterion λ_{\min} , which imposes a lower bound on $\lambda_1^{(\alpha)}$ for each condensed phase α . By satisfying the constraints of this convex optimization problem, we identify a “solution space” of pairwise interaction matrices that closely approximate the target free-energy landscape. Importantly, convexity implies that this solution space can be efficiently computed, or otherwise proven to be infeasible if solutions to the inverse design problem do not exist [42–44].

Within this solution space of pairwise interaction matrices, we wish to find a matrix with the fewest required number of molecular features, in accordance with Eq. (5). We therefore minimize the nuclear norm of the interaction matrix, $\|\epsilon\|_* \equiv \sum_{k=1}^N \sigma_k$, which is a convex relaxation of the matrix rank [45], subject to the aforementioned convex constraints. Including this objective function tends to reduce the magnitudes of the smallest singular values of ϵ . Moreover, minimizing $\|\epsilon\|_*$ guarantees that the solution to the convex optimization problem is unique. We can then determine an upper bound on the minimum required number of features, r , using Eq. (5), and finally construct a rank- r approximation of the interaction matrix, ϵ_r , by applying the EYM theorem.

Step 2: Factorization into molecular features. Second, having established the low-rank interaction matrix ϵ_r , we find a molecular realization of the pairwise interactions by factorizing ϵ_r according to Eq. (2). The rank of the feature interaction matrix \mathbf{u} must be exactly equal to r , so that exactly r features are required for each row vector of the molecular feature matrix \mathbf{W} . An optimal factorization is obtained by minimizing the Frobe-

nus norm of the reconstruction error,

$$\|\Delta^{\text{recon}} \epsilon\|_F \equiv \min_{\mathbf{W}, \mathbf{u}} \|\epsilon_r - \mathbf{W} \mathbf{u} \mathbf{W}^T\|_F. \quad (6)$$

Up until this point, the design approach has been agnostic to the details of the molecular features. However, the optimal factorization given by Eq. (6) must typically satisfy additional constraints. Most importantly, a physically interpretable molecular feature matrix \mathbf{W} typically has nonnegative entries, since each matrix element indicates the existence and magnitude of a distinct feature within a particular molecule. In this case, nonnegative matrix factorization (NMF) [46] must be used in place of eigenvalue decomposition when solving Eq. (6) (see SI). Further constraints may also be required depending on the specific requirements of the molecular system and the nature of the molecular features. For example, if each molecular feature represents the count of an amino acid type in a disordered polypeptide, then the elements of \mathbf{W} must be nonnegative integers. Similarly, the feature interaction matrix \mathbf{u} may either be fixed, as in the case of amino-acid interactions, or designable, as in the case of nucleic acid motifs [47]. As a concrete example, a specific heteropolymer model will be considered in detail below. Regardless of these system-specific constraints, the reconstruction error must obey $\|\Delta^{\text{recon}} \epsilon\|_F \lesssim \min_{\alpha} \eta \lambda_1^{(\alpha)}$ in order for the designed molecular mixture to form the prescribed condensed phases.

In summary, our inverse design approach establishes an upper bound on the number of distinct molecular features that are required to form multiple coexisting condensates with prescribed molecular compositions. We can then devise a specific molecular implementation, using the minimal number of molecular features, via a second optimization step. Next, we will demonstrate this two-step optimization procedure using a prototypical model of phase-separating polymers.

D. Designing phase-separating heteropolymers using a minimal number of monomer types

To demonstrate the validity of our theory (Sec. IIB) and design approach (Sec. IIC), we consider a common simulation model of sequence-dependent heteropolymers. In this model, polymer species $i = 1, \dots, N$ are linear chains of L_i monomers, which are chosen from a library of r monomer types (see SI for model details). Nonbonded monomers of types $a, b = 1, \dots, r$ interact via a cut-and-shifted Lennard-Jones (LJ) pair potential [48] with monomer diameter d . Bonded monomers interact via finite-extensible nonlinear elastic (FENE) bonds [49]. Our aim is to design the sequences of polymers with maximum degree of polymerization L_{\max} , along with the nonpositive monomer interaction matrix \mathbf{u}^{LJ} , in order to form a set of K coexisting condensates with prescribed polymer compositions.

As an illustrative example, we consider the 4-component, 3-condensed-phase mixture depicted in

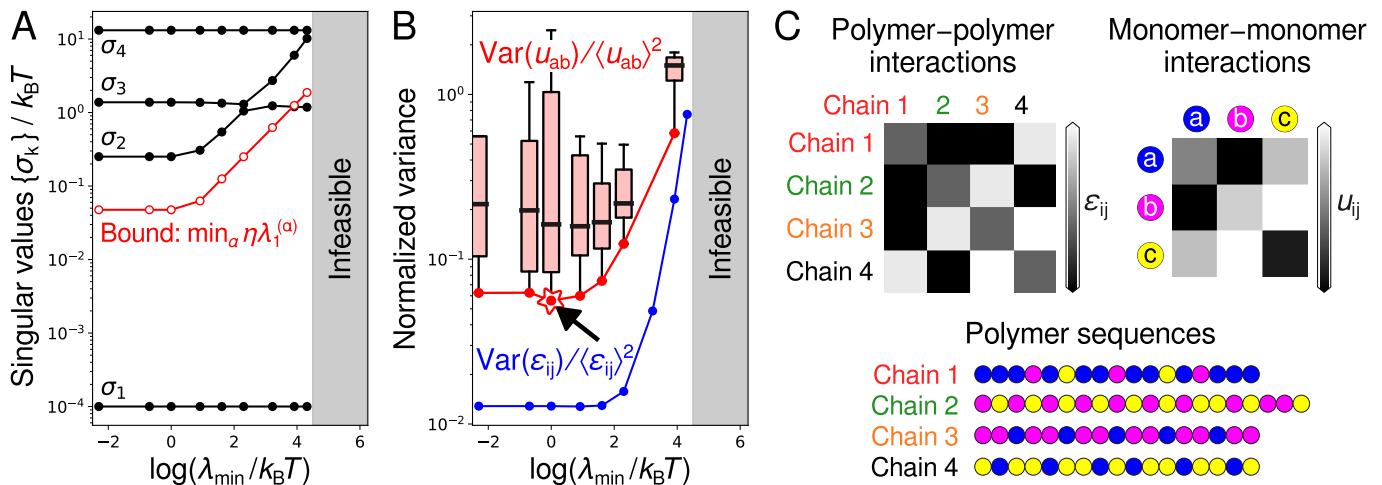


FIG. 2. **Optimization of minimal-complexity interaction matrices.** (A) Inverse design of the 4-component multiphase system illustrated in Fig. 1B. The singular values of the optimized interaction matrix ϵ , obtained via nuclear-norm minimization (Sec. II C), as a function of the landscape stability criterion λ_{\min} . The singular values tend to increase as the condensed phases become more stable. Comparing the singular values with the bound, Eq. (5), indicates that the minimum interaction matrix rank is $r = 3$. (B) The normalized pairwise interaction variance, $\text{Var}(\epsilon_{ij}) / \langle \epsilon_{ij} \rangle^2$, tends to increase with λ_{\min} . Box plots show the distribution of normalized monomer–monomer interaction variances obtained by nonnegative matrix factorization (NMF) of the optimized rank-3 polymer–polymer interaction matrices found in A, while treating the distinct monomer types as the molecular features. All NMF solutions satisfy $\|\Delta^{\text{recon}} \epsilon\|_F < \min_{\alpha} \eta \lambda_1^{(\alpha)}$. The solid red line indicates the Pareto front, representing the NMF solutions that simultaneously minimize $\text{Var}(u_{ab}) / \langle u_{ab} \rangle^2$ and maximize $\min_{\alpha} \lambda_1^{(\alpha)}$. (C) The design solution corresponding to the starred location on the Pareto front (see arrow) in B. The polymer sequences consist of exactly $r = 3$ monomer types.

Fig. 1B, which represents a nontrivial design problem due to the “enrichment” (i.e., high target volume fractions) of chains A and B in two distinct, immiscible condensed phases. Because we are designing linear polymers, we utilize the Flory–Huggins expression for the steric term in Eq. (1), $\mu_{v,i}(\phi) / k_B T = -\log(1 - \phi_T) - (1 - 1/L_i)$, where $\phi_T \equiv \sum_{i=1}^N \phi_i$ (see SI). In what follows, we choose the maximum degree of polymerization to be $L_{\max} = 20$. By solving the minimum-nuclear-norm convex optimization problem as a function of the minimum thermodynamic stability criterion, λ_{\min} (Sec. II C), we obtain the singular values of the optimized pair interaction matrix, ϵ , for this design problem (Fig. 2A). The nuclear norm of the optimized ϵ tends to increase with λ_{\min} , up to the point at which the design problem becomes infeasible, since imposing a stricter constraint on the free-energy landscape tends to shrink the interaction-matrix solution space. Accordingly, the singular values of ϵ tend to increase with λ_{\min} . We then compare the singular values with the right-hand side of Eq. (5), assuming a composition tolerance of $\eta = 20\%$. Since one singular value lies below the bound in Fig. 2A, Eq. (5) predicts that one singular value can be eliminated while still satisfying the design problem. Thus, only $r = 3$ molecular features are required for the construction of this particular heteropolymer mixture.

We now assume that the molecular features represent distinct monomer types in the LJ heteropolymer model. In this case, each row of the $N \times r$ \mathbf{W} matrix is a count encoding of the number of occurrences of each monomer

type in a heteropolymer sequence; consequently, all elements of \mathbf{W} are nonnegative integers, and the row sums of \mathbf{W} are bounded by the maximum degree of polymerization L_{\max} . Meanwhile, \mathbf{u}^{LJ} is a nonpositive $r \times r$ interaction matrix determined by the attractive portion of the monomer–monomer LJ pair potential (see SI). Here, assuming that the molecular features represent distinct monomer types is equivalent to a pairwise-additive approximation for the polymer–polymer interactions, such that $\epsilon_{ij} = \sum_{a,b} W_{ia} u_{ab}^{\text{LJ}} W_{jb}$. We emphasize that this approximation is not required by our theory, since we could instead factorize ϵ via an eigendecomposition of pairwise polymer–polymer interactions determined directly from simulations. However, we choose to make this assumption here to provide a transparent proof of principle. We note that this approximation establishes an upper bound on the required number of distinct monomer types, since the number of molecular features obtained from an eigendecomposition of ϵ cannot be less than the number of distinct monomer types. In other words, while we can use this approximation to rigorously test our theory, the bound on the required number of monomer types could potentially be improved by relaxing this assumption.

Our next step is to solve Eq. (6) subject to the optimized low-rank interaction matrix, ϵ_r , and the constraints on \mathbf{W} and \mathbf{u} . This mixed-integer quadratic nonnegative matrix factorization (NMF) problem [46] can be solved using a stochastic optimization algorithm [50]. Specifically, we generate an ensemble of \mathbf{W} matrices and iteratively solve for the interaction matrix \mathbf{u} to en-

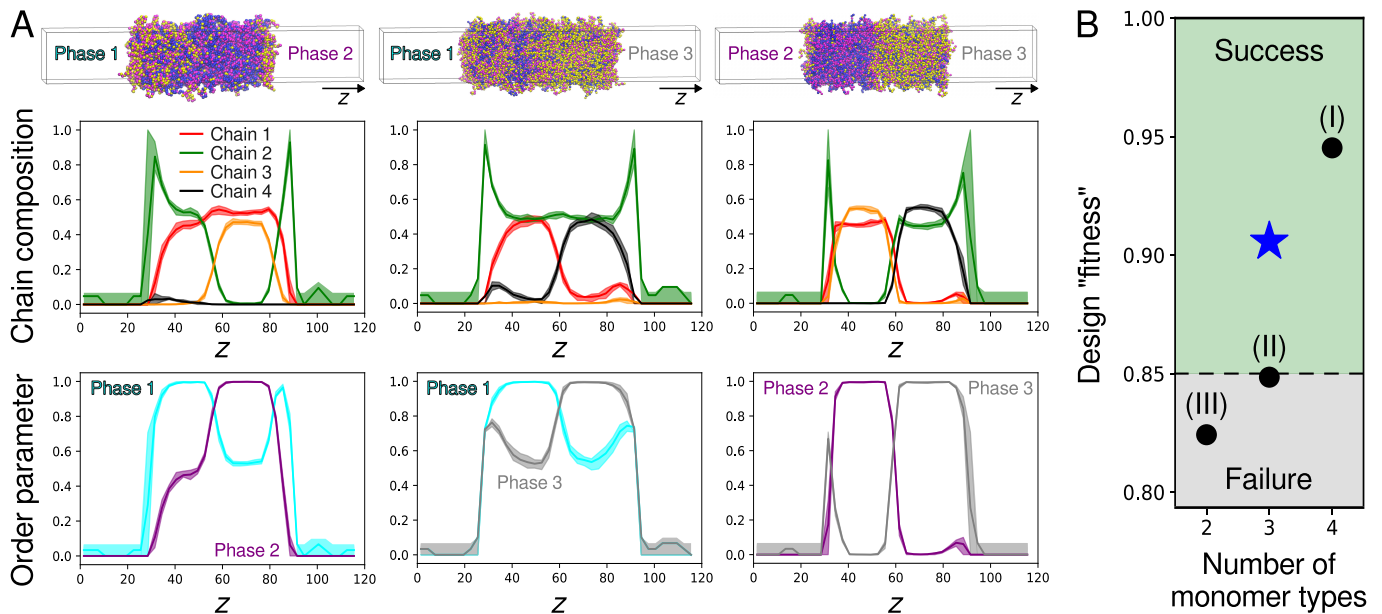


FIG. 3. **Validation of minimal-complexity heteropolymer designs via molecular simulation.** (A) Direct-coexistence simulations of all pairs of condensed phases illustrated in Fig. 1B using the 3-monomer-type heteropolymer design shown in Fig. 2C. *Top*: Equilibrium configurations, color-coded by monomer type. *Middle*: Trajectory-averaged chain composition profiles along the direction of the simulation box perpendicular to the condensate interfaces. *Bottom*: Corresponding trajectory-averaged order parameter profiles, Eq. (7). Shaded regions indicate the statistical uncertainty associated with the mean profiles. (B) Comparison of the “fitness” metric (Sec. II E) for the heteropolymer design studied in A (blue star) and three alternative designs (black circles): (I) a 4-monomer-type design chosen to maximize the condensed-phase stabilities, (II) a 3-monomer-type design constructed by applying the EYM theorem to an interaction matrix that was *not* obtained via nuclear-norm minimization, and (III) a two-monomer-type design constructed by applying NMF with $r = 2$ (see SI for complete details of these alternative designs). Designs are classified as successes or failures based on a fitness threshold of 0.85 (see SI).

sure nonpositivity; we then utilize enhanced sampling to probe the tail of the reconstruction-error distribution to find the \mathbf{W} matrix with the smallest $\|\Delta^{\text{recon}}\epsilon\|_F$ (see SI). Representative results of this stochastic algorithm are shown in Fig. 2B. We find that the relative variance of the optimized monomer–monomer interactions, $\text{Var}(u_{ab})/\langle u_{ab} \rangle^2$, tends to increase with the minimum stability constraint λ_{\min} . This trend reflects the behavior of the polymer–polymer interaction matrix, ϵ_r , that is being factorized, $\text{Var}(\epsilon_{ij})/\langle \epsilon_{ij} \rangle^2$, and suggests a fundamental trade-off: Designing highly stable condensates, which are least sensitive to interaction-matrix perturbations according to Eq. (3), requires highly dissimilar monomer–monomer interactions.

Finally, we use an optimized monomer-composition matrix, \mathbf{W} , and monomer–monomer interaction matrix, \mathbf{u}^{LJ} , to construct a set of heteropolymer sequences for simulation. Because the pairwise-additive approximation relating ϵ_{ij} and u_{ab}^{LJ} is most accurate when $\text{Var}(u_{ab})/\langle u_{ab} \rangle^2$ is small, we select monomer designs from the Pareto front shown in Fig. 2B. We then compose the polymer sequences from the monomer compositions by interleaving the different monomer types to minimize the blockiness of each sequence (see SI). An example outcome of this algorithm, which we will directly test via molecular simulation, is shown in Fig. 2C.

E. Validating multicomponent, multiphase heteropolymer designs via molecular simulation

To test our LJ heteropolymer designs, we perform direct-coexistence molecular dynamics simulations [51] to examine the molecular compositions and immiscibility of the target condensates. In these simulations, all chain types are present in a constant-temperature, constant-volume simulation with periodic boundary conditions. However, the initial condition is chosen such that two different condensed phases, $\alpha \neq \beta$, are in contact with one another and also with a dilute phase. The condensed phases are thermodynamically stable if they remain phase-separated and immiscible once the simulation has relaxed to equilibrium; in practice, we ensure convergence by calculating simulation trajectories that are many times longer than the time required for all the chains in an $\alpha = \beta$ control simulation to mix completely (see SI). We carry out simulations for all pairs of condensed phases $\alpha \neq \beta$ to confirm that they are mutually immiscible.

In Fig. 3A, we show equilibrium configurations of simulations and polymer composition profiles for the LJ heteropolymer design shown in Fig. 2C. We define an order parameter for each phase α based on the cosine similarity

of the local polymer composition $\vec{\phi}$,

$$q^{(\alpha)}(\vec{\phi}) \equiv \frac{\vec{\phi} \cdot \vec{\phi}^{(\alpha)}}{\|\vec{\phi}\| \|\vec{\phi}^{(\alpha)}\|}, \quad (7)$$

to distinguish the coexisting condensed phases (Fig. 3A). This order parameter is equal to one if the polymer composition of an equilibrated condensed phase matches that of target phase α . When coexisting condensed phases have “shared” components, meaning that one or more polymer species are enriched in multiple phases, the order parameters are not orthogonal, such that $q^{(\alpha)}(\vec{\phi}^{(\beta)}) > 0$. The order parameter profiles shown in Fig. 3A indicate that our 3-monomer-type LJ heteropolymer mixture indeed solves the design problem presented in Fig. 1B.

We can compare alternative heteropolymer designs by introducing a “fitness” metric computed from the order parameter profiles given by Eq. (7) (see SI). Using the fact that the minimum fitness of a valid solution is ≈ 0.85 (see SI), we can quantitatively assess whether each design is successful (Fig. 3B). The optimized 3-monomer-type design shown in Fig. 3A is classified as a success as expected, as is a 4-monomer-type design that has zero reconstruction error since the matrix factorization step, Eq. (6), is not required. By contrast, a 3-monomer-type design constructed by applying the EYM theorem to an interaction matrix that was *not* optimized to minimize $\|\epsilon\|_*$, and thus does not satisfy Eq. (5), fails this test. Similarly, performing NMF to solve Eq. (6) using only two monomer types leads to a large reconstruction error that violates Eq. (5), and the simulated condensed phases are observed to mix. Although this empirical test does not preclude the possibility of a successful two-monomer-type design that manifests three molecular features via sequence-patterning effects, it is consistent with our prediction that three monomer types are required if the monomer types are assumed to be the features in the heteropolymer design step. (Detailed descriptions of these alternative designs and accompanying simulation data are provided in the SI.) Finally, we note that interesting interfacial effects, particularly between the condensed and dilute phases, are more prominent in the optimized 3-monomer-type design (Fig. 3A) than in the 4-monomer-type design. This behavior is not inconsistent with our theory or design approach, which focus solely on the molecular compositions of bulk phases, and likely reflects the reduced condensed-phase stabilities (and thus lowered surface tensions) of the 3-monomer-type design.

F. Evaluating the pairwise approximation using simulations of successful condensate designs

Given the successful simulation test of our 3-monomer-type heteropolymer mixture, it is important to examine why our design approach works so well. Specifically, we can assess the pairwise-additive approximation for the polymer–polymer interactions, which is invoked when

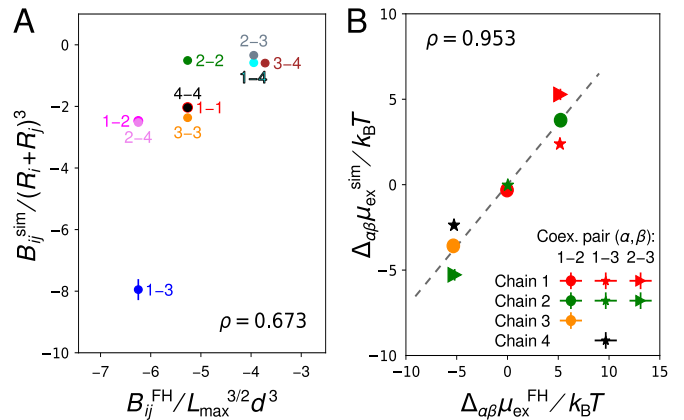


FIG. 4. Validation of the pairwise-additive approximation for polymer–polymer interactions. (A) Correlation between the second virial coefficients obtained from simulations and predicted by the Flory–Huggins (FH) model. Labels indicate chain pairs. Simulated coefficients are normalized by $(R_i + R_j)^3$, where R_i is the radius of gyration of chain i in isolation, while predicted coefficients are normalized by the pervaded volume of an ideal polymer with chain length L_{\max} [38]. (B) Correlation between the excess chemical potential differences measured in direct-coexistence simulations and predicted by the FH model. Points are shown for individual species in coexisting condensed phase pairs, α – β . The Pearson correlation coefficient, ρ , is shown for each panel.

treating the monomer types as the molecular features, directly via simulation. We first consider the interactions between polymers in a dilute mixture. These interactions are quantified by computing the second virial coefficients between polymers, B_{ij}^{sim} , and compared to the second virial coefficients predicted by the Flory–Huggins model, B_{ij}^{FH} . We find that B_{ij}^{sim} and B_{ij}^{FH} are positively correlated with a Pearson correlation coefficient of 0.67, which suggests non-negligible differences between the dilute-phase polymer–polymer interactions and the predictions of the pairwise-additive approximation (Fig. 4A).

By contrast, we find strong evidence that the pairwise-additive approximation holds to a greater extent in the condensed phases. We extract the excess chemical potential differences, $\Delta_{\alpha\beta}\mu_{\text{ex},i}^{\text{sim}} \equiv \mu_{\text{ex},i}^{(\beta)} - \mu_{\text{ex},i}^{(\alpha)}$, where the excess chemical potential is $\mu_{\text{ex},i} \equiv \mu_i - \mu_{\text{id},i}$, from the equilibrium compositions of simulated α and β bulk phases [25] and compare with the Flory–Huggins prediction, $\Delta_{\alpha\beta}\mu_{\text{ex},i}^{\text{FH}}$ (see SI). These measurements, which directly probe the accuracy of the pairwise approximation, Eq. (1), in the condensed phases, result in a much higher Pearson correlation coefficient of 0.93 (Fig. 4B). This result suggests that the polymer–polymer interactions are more mean-field-like in condensed phases, as originally pointed out by Flory [52]. More specifically, this observation suggests that the pairwise approximations for $\vec{\mu}$, Eq. (1), and ϵ (Sec. IID) work well because the overlap parameter of our LJ heteropolymers is large in the condensed phases ($P \approx 13 \pm 2$) [38].

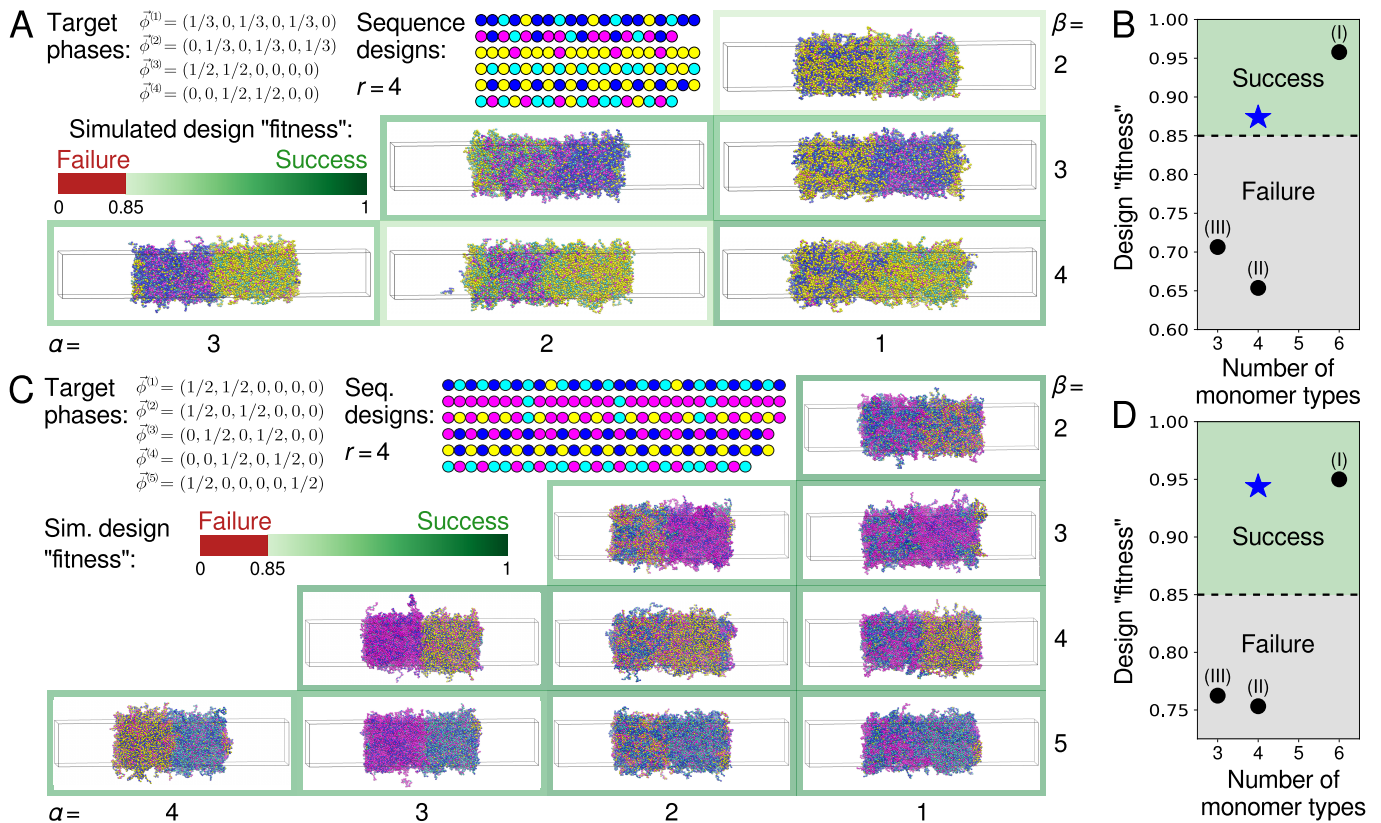


FIG. 5. **Design of complex multicomponent, multiphase condensates.** (A) Inverse design and simulation validation of a 6-component, 4-condensed-phase system with the indicated target-phase molecular volume fractions. Sequence designs use the minimal required number of monomer types, $r = 4$. Equilibrium configurations of α - β direct-coexistence simulations are shown as in Fig. 3A, and the fitness metric is indicated by the border color. (B) Comparison of the optimized design shown in A with alternative designs, as in Fig. 3B. The alternative designs (I) maximize the stability of the condensed phases using six monomer types, (II) apply the EYM theorem without nuclear-norm minimization, and (III) apply NMF with $r = 3$ monomer types. (C) Inverse design and simulation validation of a 6-component, 5-condensed-phase system with the indicated target-phase molecular volume fractions. Here, the minimal required number of monomer types is also $r = 4$. (D) Comparison of the optimized design shown in C with alternative designs. Complete data for all designs are provided in the SI.

In line with our analysis of the excess chemical potentials, we find that the microstructures of the condensed phases agree with expectations based on the Gaussian Core Model (GCM) of finite-length polymers [53]. From simulations of individual, homogeneous condensed phases, we obtain the radial distribution function (RDF) for the center of mass of the polymer chains (see SI). Consistent with the GCM, the RDFs for all polymer species pairs exhibit a correlation hole, meaning that the centers of mass overlap with low probability, while a positive peak is found at a distance of approximately twice the radius of gyration, implying effective attractions between chains. The amplitudes of these peaks anticorrelate with the predicted pairwise interaction strengths given by ϵ . Most tellingly, the zero-wavenumber structure factor, which can be directly related to the pairwise interactions [37] (see SI), exhibits a Pearson correlation coefficient of 0.997 with respect to the predictions of the pairwise approximation. Thus, overall, our simulations provide a convincing *post hoc* validation of the key ap-

proximations utilized in applying our inverse design strategy to sequence-dependent LJ heteropolymers.

G. Designing minimal-complexity biomolecular mixtures with complex phase behavior

The theory and inverse design approach that we describe here are broadly applicable for understanding complex, multiphase coexistence in biomolecular mixtures. To demonstrate its generality, we apply our inverse design approach to two additional interesting design problems, and then verify our predictions using simulations of LJ heteropolymers (see SI for complete details).

First, we consider a 6-component mixture in which components are shared among four condensed phases (Fig. 5A). This design problem is interesting because the number of enriched components differs among the condensed phases. Following the approach described in Sec. IID, we predict that at most $r = 4$ monomer types

are required to construct LJ heteropolymers that phase separate into the prescribed phases. Performing simulations of all pairs of condensed phases as described in Sec. II E confirms this prediction, where we use the previously described fitness metric to assess the result of each phase pair. We also consider alternative designs in Fig. 5B, where we compare the minimum fitness of all phase pairs. These results are consistent with the predicted minimum number of monomer types and highlight the importance of following our inverse design algorithm to obtain a successful minimal-complexity design.

Second, we examine a scenario in which a 6-component mixture forms five condensed phases with shared components (Fig. 5C). Surprisingly, we find that the required number of molecular features, $r = 4$, is not only smaller than the number of components, but is also smaller than the number of condensed phases. To solve the matrix factorization problem, Eq. (6), we find that it is necessary to increase the maximum degree of polymerization to $L_{\max} = 30$. Our simulations of designed LJ heteropolymers (Fig. 5C) and comparisons to alternative designs (Fig. 5D) similarly support our prediction that at most four monomer types are required to achieve the desired phase behavior. Taken together, these additional examples demonstrate the generality of our design approach and suggest that scenarios in which complex phase behavior can be realized using a small number of molecular features are not particularly rare.

III. DISCUSSION

Our accomplishments in this paper are twofold. First, we establish a relationship between multiphase condensates and the complexity of the pairwise interactions in a biomolecular mixture. Specifically, we show that achieving multiphase organization via phase separation requires a minimal number of distinct molecular features, which represent linearly independent modes of interaction in a biomolecular mixture. While the physicochemical nature of these features may differ between different types of biomolecules, such as disordered proteins [54], nucleic acids [55], and multi-domain proteins [56], the required number of molecular features is determined solely by the target phase behavior. Second, we develop a two-step inverse design algorithm for calculating an upper bound on the required number of molecular features and then constructing minimal-complexity biomolecular mixtures that achieve the target phase behavior. We apply this inverse design approach to construct mixtures of model Lennard-Jones (LJ) heteropolymers that phase-separate into nontrivial coexisting phases, which would be extremely difficult to obtain without a rational design algorithm. Extensive molecular dynamics simulations provide direct support for the validity of our theory and inverse design approach, as well as justification for the additional approximations employed when applying our design approach to the LJ heteropolymer model.

Our results demonstrate that complex multiphase organization can be achieved using a relatively small number of chemical building blocks. On the one hand, this observation should not be surprising given the diversity of compositionally distinct phase-separated condensates that have been observed in living cells. Yet on the other hand, the way in which relatively “promiscuous” interactions among conformationally disordered biomolecules give rise to many immiscible condensates with controlled molecular compositions has been unclear until now. We speculate that the difference between the number of components in a mixture and the required number of molecular features will only tend to increase as the number of the components and the number of condensed phases grow. We reiterate that the number of monomer types computed in our studies of LJ heteropolymers represents an *upper bound* on the required number of monomer types, since the number of molecular features that govern interactions between linear polymers can exceed the number of monomer types. For example, it is well known that sequence-dependent properties, such as sequence “blockiness” [17, 57] and charge-patterning effects [58–61], tune the phase behavior of heteropolymer solutions in ways that cannot be predicted the monomer composition of the heteropolymers alone. In future work, we will incorporate such sequence-dependent features into our inverse design approach in order to tighten the bound on the required number of monomer types and broaden the range of applicability of our heteropolymer design algorithm. Overall, we hope that our approach will provide a unifying framework for recent efforts to identify molecular “grammars” governing phase separation in specific biomolecular systems [14–18].

Our two-step inverse design algorithm also establishes an extensible framework for designing phase-separating multicomponent fluids using a wide variety of synthetic building blocks. The key requirement is specifying the system-specific constraints on the molecular feature matrix and the feature–feature interactions. For example, we could apply our theory to design “patchy” colloidal particles [62], in which case the feature matrix indicates the surface area covered by a sticker type and the feature–feature interactions represent the interactions between different types of stickers. Nonetheless, we caution that making simplifying assumptions regarding the molecular interactions, such as the pairwise-additive approximation employed for LJ heteropolymers, are most likely to work well in systems with large overlap parameters; otherwise, the accuracy of the design algorithm is likely to be sensitive to the definitions of the molecular features and the way in which the molecular interactions are modeled.

In conclusion, our theory and inverse design approach advance our understanding of multiphase condensate formation in biology, as well as our ability to engineer chemically diverse artificial condensates. Our predictions could be tested using existing experimental technologies in both biological [54, 63–67] and synthetic [68–71] systems. Ultimately, by incorporating the design of tunable

interfacial tensions [72, 73] and nonequilibrium chemical activity [74, 75] into our framework, it will be possible to realize fully “programmable” fluids and soft materials that self-organize via multicomponent phase separation.

ACKNOWLEDGMENTS

The authors acknowledge Ofer Kimchi, Isabella Graf, and Zhuang Liu for providing comments on a previous version of this manuscript and Princeton Research Computing for technical support. Source code and example calculations can be found at <https://github.com/wmjac/phaseprogramming-pub>.

-
- [1] A. A. Hyman, C. A. Weber, and F. Jülicher, *Ann. Rev. Cell Dev. Biol.* **30**, 39 (2014).
- [2] Y. Shin and C. P. Brangwynne, *Science* **357**, eaaf4382 (2017).
- [3] J. Berry, C. P. Brangwynne, and M. Haataja, *Rep. Prog. Phys.* **81**, 046601 (2018).
- [4] S. Alberti, A. Gladfelter, and T. Mittag, *Cell* **176**, 419 (2019).
- [5] S. F. Banani, H. O. Lee, A. A. Hyman, and M. K. Rosen, *Nat. Rev. Mol. Cell Bio.* **18**, 285 (2017).
- [6] W. Xing, D. Muhrad, R. Parker, and M. K. Rosen, *Elife* **9**, e56525 (2020).
- [7] H. R. Kilgore and R. A. Young, *Nat. Chem. Biol.* **18**, 1298 (2022).
- [8] X. Su, J. A. Ditlev, E. Hui, W. Xing, S. Banjade, J. Okrut, D. S. King, J. Taunton, M. K. Rosen, and R. D. Vale, *Science* **352**, 595 (2016).
- [9] L. B. Case, J. A. Ditlev, and M. K. Rosen, *Ann. Rev. Biophys.* **48**, 465 (2019).
- [10] D. L. Lafontaine, J. A. Riback, R. Bascetin, and C. P. Brangwynne, *Nat. Rev. Mol. Cell Biol.* , 1 (2020).
- [11] D. W. Sanders, N. Kedersha, D. S. Lee, A. R. Strom, *et al.*, *Cell* **181**, 306 (2020).
- [12] M.-T. Wei, Y.-C. Chang, S. F. Shimobayashi, Y. Shin, A. R. Strom, and C. P. Brangwynne, *Nat. Cell Biol.* **22**, 1187 (2020).
- [13] H. Lyons, R. T. Veettil, P. Pradhan, C. Fornero, N. De La Cruz, K. Ito, M. Eppert, R. G. Roeder, and B. R. Sabari, *Cell* **186**, 327 (2023).
- [14] C. P. Brangwynne, P. Tompa, and R. V. Pappu, *Nat. Phys.* **11**, 899 (2015).
- [15] F. G. Quiroz and A. Chilkoti, *Nat. Mater.* **14**, 1164 (2015).
- [16] J. Wang, J.-M. Choi, A. S. Holehouse, H. O. Lee, X. Zhang, M. Jahnel, S. Maharana, R. Lemaitre, A. Pozniakovsky, D. Drechsel, I. Poser, R. V. Pappu, S. Alberti, and A. A. Hyman, *Cell* **174**, 688 (2018).
- [17] E. W. Martin, A. S. Holehouse, I. Peran, M. Farag, J. J. Incicco, A. Bremer, C. R. Grace, A. Soranno, R. V. Pappu, and T. Mittag, *Science* **367**, 694 (2020).
- [18] S. Rekhi, C. G. Garcia, M. Barai, A. Rizuan, B. S. Schuster, K. L. Kiick, and J. Mittal, *Expanding the molecular language of protein liquid-liquid phase separation*, preprint (2023).
- [19] T. S. Harmon, A. S. Holehouse, M. K. Rosen, and R. V. Pappu, *Elife* **6**, e30294 (2017).
- [20] G. L. Dignon, R. B. Best, and J. Mittal, *Ann. Rev. Phys. Chem.* **71**, 53 (2020).
- [21] J. A. Villegas, M. Heidenreich, and E. D. Levy, *Nat. Chem. Biol.* **18**, 1319 (2022).
- [22] R. V. Pappu, S. R. Cohen, F. Dar, M. Farag, and M. Kar, *Chem. Rev.* (2023).
- [23] J. A. Ditlev, L. B. Case, and M. K. Rosen, *J. Mol. Biol.* **430**, 4666 (2018).
- [24] A. Musacchio, *EMBO J.* **41**, e109952 (2022).
- [25] W. M. Jacobs, *J. Chem. Theory Comput.* **19**, 3429 (2023).
- [26] W. M. Jacobs and D. Frenkel, *Biophys. J.* **112**, 683 (2017).
- [27] W. M. Jacobs, *Phys. Rev. Lett.* **126**, 258101 (2021).
- [28] F. Chen and W. M. Jacobs, *J. Chem. Phys.* **158**, 214118 (2023).
- [29] T. S. Harmon, A. S. Holehouse, and R. V. Pappu, *New J. Phys.* **20**, 045002 (2018).
- [30] S. Mao, D. Kuldinow, M. P. Haataja, and A. Košmrlj, *Soft Matter* **15**, 1297 (2019).
- [31] J. R. Espinosa, J. A. Joseph, I. Sanchez-Burgos, A. Garaizar, D. Frenkel, and R. Collepardo-Guevara, *Proc. Natl. Acad. Sci. U.S.A.* **117**, 13238 (2020).
- [32] K. Shrinivas and M. P. Brenner, *Proc. Natl. Acad. Sci. U.S.A.* **118**, e2108551118 (2021).
- [33] D. Zwicker and L. Laan, *Proc. Natl. Acad. Sci. U.S.A.* **119**, e2201250119 (2022).
- [34] I. R. Graf and B. B. Machta, *Phys. Rev. Research* **4**, 033144 (2022).
- [35] G. Carugno, I. Neri, and P. Vivo, *Phys. Biol.* (2022).
- [36] F. C. Thewes, M. Krüger, and P. Sollich, *Phys. Rev. Lett.* **131**, 058401 (2023).
- [37] J.-P. Hansen and I. R. McDonald, *Theory of simple liquids: With applications to soft matter* (Academic Press, 2013).
- [38] R. H. Colby and M. Rubinstein, *Polymer physics* (Oxford University Press, 2003).
- [39] D. A. Porter and K. E. Easterling, *Phase transformations in metals and alloys* (CRC press, 2009).
- [40] J. Wessén, S. Das, T. Pal, and H. S. Chan, *J. Phys. Chem. B* **126**, 9222 (2022).
- [41] C. Eckart and G. Young, *Psychometrika* **1**, 211–218 (1936).
- [42] S. P. Boyd and L. Vandenberghe, *Convex optimization* (Cambridge University Press, 2004).
- [43] S. Diamond and S. Boyd, *J. Mach. Learn. Res.* **17**, 2909 (2016).
- [44] B. O’Donoghue, E. Chu, N. Parikh, and S. Boyd, *J. Optimiz. Theory App.* **169**, 1042 (2016).
- [45] B. Recht, M. Fazel, and P. A. Parrilo, *SIAM Review* **52**, 471–501 (2010).
- [46] Z. Yang and E. Oja, *Pattern Recognition* **45**, 1500 (2012).
- [47] J. SantaLucia, *Proc. Natl. Acad. Sci. U.S.A.* **95**, 1460 (1998).

- [48] J. E. Lennard-Jones, Proc. Royal Soc. A **106**, 463–477 (1924).
- [49] K. Kremer and G. S. Grest, J. Chem. Phys. **92**, 5057–5086 (1990).
- [50] P.-T. De Boer, D. P. Kroese, S. Mannor, and R. Y. Rubinstein, Ann. Oper. Res. **134**, 19 (2005).
- [51] S. Plimpton, J. Comput. Phys. **117**, 1 (1995).
- [52] P.-G. De Gennes, *Scaling concepts in polymer physics* (Cornell University Press, 1979).
- [53] A. A. Louis, P. G. Bolhuis, and J. P. Hansen, Phys. Rev. E **62**, 7961 (2000).
- [54] J. R. Simon, N. J. Carroll, M. Rubinstein, A. Chilkoti, and G. P. López, Nat. Chem. **9**, 509 (2017).
- [55] A. Jain and R. D. Vale, Nature **546**, 243 (2017).
- [56] P. Li, S. Banjade, H.-C. Cheng, S. Kim, B. Chen, L. Guo, M. Llaguno, J. V. Hollingsworth, D. S. King, S. F. Banani, *et al.*, Nature **483**, 336 (2012).
- [57] U. Rana, C. P. Brangwynne, and A. Z. Panagiotopoulos, J. Chem. Phys. **155**, 125101 (2021).
- [58] R. K. Das and R. V. Pappu, Proc. Natl. Acad. Sci. U.S.A. **110**, 13392 (2013).
- [59] Y.-H. Lin, J. D. Forman-Kay, and H. S. Chan, Phys. Rev. Lett. **117**, 178101 (2016).
- [60] T. Pal, J. Wessén, S. Das, and H. S. Chan, Phys. Rev. E **103**, 042406 (2021).
- [61] P. Y. Chew, J. A. Joseph, R. Collepardo-Guevara, and A. Reinhardt, Chem. Sci. **14**, 1820 (2023).
- [62] S. C. Glotzer and M. J. Solomon, Nat. Mater. **6**, 557 (2007).
- [63] S. Boeynaems, A. S. Holehouse, V. Weinhardt, D. Kovacs, J. Van Lindt, C. Larabell, L. Van Den Bosch, R. Das, P. S. Tompa, R. V. Pappu, *et al.*, Proc. Natl. Acad. Sci. U.S.A. **116**, 7889 (2019).
- [64] R. S. Fisher and S. Elbaum-Garfinkle, Nat. Commun. **11**, 4628 (2020).
- [65] T. Kaur, M. Raju, I. Alshareedah, R. B. Davis, D. A. Potoyan, and P. R. Banerjee, Nat. Commun. **12**, 872 (2021).
- [66] A. Baruch Leshem, S. Sloan-Dennison, T. Massarano, S. Ben-David, D. Graham, K. Faulds, H. E. Gottlieb, J. H. Chill, and A. Lampel, Nat. Commun. **14**, 421 (2023).
- [67] M. T. Walls, K. Xu, C. P. Brangwynne, and J. L. Avalos, *A Modular Design for Synthetic Membraneless Organelles Enables Compositional and Functional Control*, preprint (2023).
- [68] Y. Dai, L. You, and A. Chilkoti, Nat. Rev. Bioeng. **1**, 466 (2023).
- [69] T. Lu and E. Spruijt, J. Am. Chem. Soc. **142**, 2905 (2020).
- [70] S. Do, C. Lee, T. Lee, D.-N. Kim, and Y. Shin, Sci. Adv. **8**, eabj1771 (2022).
- [71] X. Liu, A. H. Mokarizadeh, A. Narayanan, P. Mane, A. Pandit, Y.-M. Tseng, M. Tsige, and A. Joy, J. Am. Chem. Soc. (2023).
- [72] S. Mao, M. S. Chakraverti-Wuerthwein, H. Gaudio, and A. Košmrlj, Phys. Rev. Lett. **125**, 218003 (2020).
- [73] T. Li and W. M. Jacobs, arXiv (2023).
- [74] Y. Cho and W. M. Jacobs, Phys. Rev. Lett. **130**, 128203 (2023).
- [75] Y. Cho and W. M. Jacobs, J. Chem. Phys. **159** (2023).

SUPPLEMENTARY INFORMATION FOR
“EMERGENCE OF MULTIPHASE CONDENSATES FROM A LIMITED SET OF CHEMICAL
BUILDING BLOCKS”

I. RELATING INTERACTION INTERDEPENDENCIES AND BIOMOLECULAR CONDENSATE
THERMODYNAMICS

A. Multicomponent macromolecular solutions with pairwise interactions

Throughout this work, we consider a solution of N macromolecular species in an implicit solvent. The concentrations (i.e., number densities) of the macromolecular species, $\{\rho_i\}$, are related to the macromolecular volume fractions, $\{\phi_i \equiv v_i \rho_i\}$, by the macromolecular excluded volumes, $\{v_i\}$. As discussed in the main text, we assume a free-energy density f in which the molecular interactions follow a pairwise approximation. This means that the (scaled) chemical potentials of all macromolecular components, $\mu_i = \partial f / \partial \phi_i = v_i^{-1} \partial f / \partial \rho_i$, can be described by the equation

$$\mu_i(\vec{\phi}) = \mu_{\text{id},i}(\vec{\phi}) + \mu_{\text{v},i}(\vec{\phi}) + \sum_{j=1}^N \epsilon_{ij} \phi_j, \quad (\text{S1})$$

where $\mu_{\text{id},i} = v_i^{-1} k_B T \log \phi_i$ is the ideal contribution to the chemical potential and $\mu_{\text{v},i}(\vec{\phi})$ accounts for steric contributions. Note that the chemical potential of macromolecular species i , as defined above, is scaled with respect to the excluded volume v_i ; this choice is made for convenience and does not affect our results. Both the ideal and the steric contributions are independent of the pairwise interaction matrix, ϵ . Meanwhile, the pairwise interaction matrix, ϵ , is assumed to be independent of the macromolecular concentrations.

B. Perturbative analysis of the landscape stability

Applying small perturbations to the component-wise interactions $\{\epsilon_{ij}\}$, we expand the free-energy density, f , to linear order,

$$\tilde{f} = f + \sum_{i=1}^N \sum_{j=i}^N \frac{\partial f}{\partial \epsilon_{ij}} \Delta \epsilon_{ij} + \sum_{i=1}^N \frac{\partial f}{\partial \phi_i} \Delta \phi_i. \quad (\text{S2})$$

Since ϵ is a symmetric $N \times N$ matrix, we only consider the independent degrees of freedom $\{\epsilon_{ij}\}$ for which $i \leq j$. Eq. (S1) implies that $\partial f / \partial \epsilon_{ij} = (1/2)^{\delta_{ij}} \phi_i \phi_j$. We can therefore rewrite the term in Eq. (S2) involving $\Delta \epsilon_{ij}$ in matrix–vector notation,

$$\begin{aligned} \sum_{i=1}^N \sum_{j=i}^N \frac{\partial f}{\partial \epsilon_{ij}} \Delta \epsilon_{ij} &= \frac{1}{2} \left(\sum_{i=1}^N \phi_i \Delta \epsilon_{ii} \phi_i + 2 \sum_{i < j} \phi_i \Delta \epsilon_{ij} \phi_j \right) \\ &= \frac{1}{2} \left(\sum_{i=1}^N \phi_i \Delta \epsilon_{ii} \phi_i + \sum_{i < j} \phi_i \Delta \epsilon_{ij} \phi_j + \sum_{i > j} \phi_i \Delta \epsilon_{ij} \phi_j \right) \\ &= \frac{1}{2} \vec{\phi}^\top \Delta \epsilon \vec{\phi}. \end{aligned} \quad (\text{S3})$$

We then expand the chemical potentials at phase coexistence,

$$\tilde{\mu}_k = \mu_k + \sum_{j=i}^N \sum_{i=1}^N \frac{\partial^2 f}{\partial \epsilon_{ij} \partial \phi_k} \Delta \epsilon_{ij} + \sum_{i=1}^N \frac{\partial^2 f}{\partial \phi_k \partial \phi_i} \Delta \phi_i. \quad (\text{S4})$$

The change in the chemical potentials, $\Delta \vec{\mu}$, can be written in matrix–vector notation as

$$\Delta \vec{\mu} \equiv \tilde{\vec{\mu}} - \vec{\mu} = \Delta \epsilon \vec{\phi} + \left(\frac{\partial^2 f}{\partial \vec{\phi}^2} \right) \Delta \vec{\phi}. \quad (\text{S5})$$

The grand potential density in the α phase, $\tilde{\Omega}^{(\alpha)} \equiv \tilde{f} - \tilde{\mu} \cdot \vec{\phi}$, can similarly be written as

$$\begin{aligned} \tilde{\Omega}^{(\alpha)} &= \Omega^{(\alpha)} + \left. \frac{\partial f}{\partial \vec{\phi}} \right|^{(\alpha)} \cdot \Delta \vec{\phi}^{(\alpha)} + \sum_{i=1}^N \sum_{j=i}^N \left. \frac{\partial f}{\partial \epsilon_{ij}} \right|^{(\alpha)} \Delta \epsilon_{ij} - \tilde{\mu} \cdot \Delta \vec{\phi}^{(\alpha)} - \Delta \tilde{\mu}^{(\alpha)} \cdot \vec{\phi}^{(\alpha)} \\ &= \Omega^{(\alpha)} + \tilde{\mu} \cdot \Delta \vec{\phi}^{(\alpha)} + \frac{1}{2} \vec{\phi}^{(\alpha)\top} \Delta \epsilon \vec{\phi}^{(\alpha)} - \tilde{\mu} \cdot \Delta \vec{\phi}^{(\alpha)} - \Delta \tilde{\mu}^{(\alpha)} \cdot \vec{\phi}^{(\alpha)} \\ &= \Omega^{(\alpha)} + \frac{1}{2} \vec{\phi}^{(\alpha)\top} \Delta \epsilon \vec{\phi}^{(\alpha)} - \Delta \tilde{\mu}^{(\alpha)} \cdot \vec{\phi}^{(\alpha)}. \end{aligned} \quad (\text{S6})$$

At coexistence, it is required that $\tilde{\mu}^{(\alpha)} = \tilde{\mu}^{(0)}$ and $\Omega^{(\alpha)} = \Omega^{(0)}$ for every condensed phase $\alpha = 1, \dots, K$, where the index 0 indicates the dilute phase. Requiring that the perturbed phases remain at coexistence means that $\Delta \tilde{\mu}^{(\alpha)} = \Delta \tilde{\mu}^{(0)}$ and $\tilde{\Omega}^{(\alpha)} = \tilde{\Omega}^{(0)}$. Since $\Delta \tilde{\mu} = \Delta \epsilon \vec{\phi} + (\partial^2 f / \partial \vec{\phi}^2) \Delta \vec{\phi}$ from Eq. (S5), we find that the coexistence condition for $\tilde{\Omega}$ is

$$-\frac{1}{2} (\vec{\phi}^{(\alpha)} - \vec{\phi}^{(0)})^\top \Delta \epsilon (\vec{\phi}^{(\alpha)} + \vec{\phi}^{(0)}) = (\vec{\phi}^{(\alpha)} - \vec{\phi}^{(0)})^\top \left(\frac{\partial^2 f}{\partial \vec{\phi}^2} \right) \Delta \vec{\phi}. \quad (\text{S7})$$

Assuming that the dilute phase is very dilute, this result simplifies to

$$\Delta \epsilon \vec{\phi}^{(\alpha)} = -2 \left. \frac{\partial^2 f}{\partial \vec{\phi}^2} \right|^{(\alpha)} \cdot \Delta \vec{\phi}. \quad (\text{S8})$$

Eq. (S8) relates changes in the macromolecular concentrations in the α phase to perturbations in the pairwise interactions, assuming that the Hessian matrix of the α phase is known. We can then estimate the noise tolerance of the interaction matrix ϵ in the worst-case scenario by considering compositional changes along the least stable direction, $\hat{\nu}_1^{(\alpha)}$, of each target phase, where

$$\left. \frac{\partial^2 f}{\partial \vec{\phi}^2} \right|^{(\alpha)} \cdot \hat{\nu}_1^{(\alpha)} = \lambda_1^{(\alpha)} \hat{\nu}_1^{(\alpha)}, \quad (\text{S9})$$

and the eigenvalues of the Hessian matrix are $0 > \lambda_1^{(\alpha)} \geq \lambda_2^{(\alpha)} \geq \dots \geq \lambda_N^{(\alpha)}$. Projecting an arbitrary concentration change $\Delta \vec{\phi}$ onto the least stable direction, we find

$$\|\Delta \epsilon \vec{\phi}^{(\alpha)}\|_F = \eta \lambda_1^{(\alpha)}, \quad (\text{S10})$$

where $\eta \equiv 2 \Delta \vec{\phi} \cdot \hat{\nu}_1^{(\alpha)} / \|\vec{\phi}^{(\alpha)}\|$ corresponds to twice the relative percentage change of macromolecular composition in the α phase and $\|\cdot\|_F$ is the Frobenius norm. Applying the sub-multiplicative property of the Frobenius norm to the left-hand side, we have

$$\|\Delta \epsilon \hat{\phi}\|_F \leq \|\Delta \epsilon\|_F \|\hat{\phi}\|_2;$$

the equality holds if $\hat{\phi}$ and each row of $\Delta \epsilon$ are linearly independent. Assuming that this is the case, we can express the tolerance of the reconstruction error for each target phase α in terms of an allowed relative composition change η ,

$$\|\Delta \epsilon\|_F \approx \eta \lambda_1^{(\alpha)}. \quad (\text{S11})$$

The overall tolerance is therefore given by

$$\|\Delta \epsilon\|_F \approx \min_{\alpha} \eta \lambda_1^{(\alpha)}. \quad (\text{S12})$$

Based on this analysis, the optimal interaction matrix ϵ should simultaneously maximize the landscape stability and minimize the reconstruction error, $\|\Delta \epsilon\|_F$. Using Eq. (S12), we can apply the Eckart–Young–Mirsky (EYM) theorem [1] to find that the smallest number of distinct molecular features, r , that successfully solve the inverse design problem,

$$\left[\sum_{k=1}^{N-r} \sigma_k^2 \right]^{1/2} \lesssim \min_{\alpha} \eta \lambda_1^{(\alpha)}, \quad (\text{S13})$$

where $\sigma_1 \leq \sigma_2 \leq \dots \leq \sigma_N$ are the singular values of ϵ . In other words, for a given $N \times N$ interaction matrix ϵ , the rank- r approximation, ϵ_r , that minimizes $\|\Delta \epsilon\|_F = \|\epsilon_r - \epsilon\|_F$ can be obtained by eliminating the smallest $N - r$ singular values of ϵ . If these smallest singular values are nonzero, then the left-hand-side of Eq. (S13) will be nonzero, and the rank- r approximation of the interaction matrix, ϵ_r , will not exactly equal the original interaction matrix, ϵ . However, the macromolecular compositions of the resulting coexisting phases will deviate from the target compositions within the allowed tolerance η if Eq. (S13) is satisfied. Eq. (S13) thus motivates the identification of the minimal number of distinct molecular features, r , needed to stabilize a set of target phases.

II. TWO-STEP OPTIMIZATION-BASED DESIGN APPROACH

A. Convex relaxation for component-wise interactions

In order to obtain coexisting phases with prescribed macromolecular volume fractions $\{\vec{\phi}^{(1)}, \vec{\phi}^{(2)}, \dots, \vec{\phi}^{(K)}\}$, we first solve for the component-wise interactions using convex programming. We refer the reader to Ref. [2] for a detailed discussion of this approach. The convex relaxation of the thermodynamic-stability and target-volume-fraction constraints defines a semi-definite program (SDP) [3],

$$\mu_{\text{id},i}(\vec{\phi}^{(\alpha)}; \vec{v}) + \mu_{\text{ex},i}(\vec{\phi}^{(\alpha)}; \boldsymbol{\epsilon}, \vec{v}) \geq \mu_i \quad \forall i, \alpha \quad (\text{S14a})$$

$$P(\vec{\phi}^{(\alpha)}; \boldsymbol{\epsilon}, \vec{v}) = 0 \quad \forall \alpha \quad (\text{S14b})$$

$$\partial[\vec{\mu}_{\text{id}}(\vec{\phi}^{(\alpha)}; \vec{v}) + \vec{\mu}_{\text{ex}}(\vec{\phi}^{(\alpha)}; \boldsymbol{\epsilon}, \vec{v})]/\partial\vec{\phi} \succ \lambda_{\min} I \quad \forall \alpha \quad (\text{S14c})$$

$$\phi_{\text{T}}^{(0)}(\vec{\mu}; \vec{v}) < \phi_{\text{T}}^*(\vec{v}). \quad (\text{S14d})$$

Components are either “enriched” or “depleted” in the α phase, depending on whether they make a substantial or negligible contribution, respectively, to the macromolecular composition of that phase. The ideal chemical potential is $\mu_{\text{id},i} = v_i^{-1} \log \phi_i^{(\alpha)}$ for any component i that is enriched in the α phase or $\mu_{\text{id},i} = v_i^{-1} \log \phi_{\text{depl}}^{(\alpha)}$ for any component i that is depleted in the α phase. The equality(inequality) in Eq. (S14a) applies to enriched(depleted) components. The volume fraction of any component that is depleted in the α phase cannot exceed $\phi_{\text{depl}}^{(\alpha)} \equiv \zeta \phi_{\text{T}}^{(\alpha)} / [M^{(\alpha)}(N - M^{(\alpha)})]$, where $\phi_{\text{T}}^{(\alpha)}$ is the total volume compositions of all components in the α phase, $M^{(\alpha)}$ is the number of enriched components in the α phase, and ζ is an adjustable parameter. In this work, we choose $\phi_{\text{T}} = 0.9$ and $\zeta = 10^{-2}$ for all target phases. Eq. (S14b) states that the pressure, P , must be zero in all phases, since the pressure in the dilute phase, which is nearly ideal, is also approximately zero. In Eq. (S14c), the parameter $\lambda_{\min} \geq 0$ places a lower bound on the smallest eigenvalue of the Hessian matrix in order to guarantee thermodynamic stability. The final constraint, Eq. (S14d), ensures that the volume fraction in the dilute phase, $\phi_{\text{T}}^{(0)}$, is less than the critical volume fraction, $\phi_{\text{T}}^*(\vec{v})$. This condition is independent of $\boldsymbol{\epsilon}$ due to the zero-osmotic-pressure assumption. We implement and solve this SDP in practice using efficient convex-optimization software [4, 5].

Within the approximations of this convex relaxation, the constraints given by Eq. (S14) define the joint space of interaction matrices, $\boldsymbol{\epsilon}$, and chemical potential vectors, $\vec{\mu}$, for which bulk phase coexistence can be established among the target condensed phases and a dilute phase. Based on the perturbative analysis in SI Sec. IB, we choose to minimize the nuclear norm, $\|\boldsymbol{\epsilon}\|_* \equiv \sum_{i=1}^N \sigma_i$, to pick out a unique solution from within the solution space that satisfies the constraints, Eq. (S14). This objective function is a convex relaxation of the matrix rank [6] and thus tends to select $\boldsymbol{\epsilon}$ matrices with small singular values. We then identify the smallest number of molecular features, r , with which we can satisfy the bound given in Eq. (S13). Finally, we obtain the low-rank approximation $\boldsymbol{\epsilon}_r$ for the component-wise interactions via the EYM theorem. By contrast, the objective function used in Ref. [2] tends to select $\boldsymbol{\epsilon}$ with larger singular values; as a result, solutions obtained using this alternative objective function tend to require a larger number of molecular features to satisfy the bound given in Eq. (S13).

B. Stochastic optimization for feature-wise interactions

In the second step of our design approach, we aim to factorize the low-rank approximation of the component-wise interaction matrix, $\boldsymbol{\epsilon}_r$, by minimizing the reconstruction error $\|\Delta^{\text{recon}} \boldsymbol{\epsilon}\|_F$. However, we are, in general, unable to use a straightforward eigenvalue decomposition of $\boldsymbol{\epsilon}_r$, since we typically wish to interpret the factorization in terms of nonnegative molecular feature vectors. This means that we must, in general, solve a nonnegative matrix factorization (NMF) problem [7]. To this end, we specify the loss function

$$\mathcal{L} \equiv \|\Delta^{\text{recon}} \boldsymbol{\epsilon}\|_F^2 = \|\boldsymbol{\epsilon}_r - \mathbf{W} \mathbf{u} \mathbf{W}^T\|_F^2, \quad (\text{S15})$$

which is nonlinear with respect to the independent variables \mathbf{W} and \mathbf{u} . Here we consider two possible scenarios, in which the molecular feature matrix, \mathbf{W} , can either take nonnegative real values or nonnegative integers.

1. NMF without integer constraints

When there are no integer constraints on the molecular feature matrix \mathbf{W} , Eq. (S15) is biconvex with respect to either \mathbf{W} or \mathbf{u} . The NMF problem can therefore be solved by iteratively alternating optimization of \mathbf{W} and \mathbf{u} , with

guaranteed convergence to a local optimum [7]. Here we consider a scenario in which \mathbf{W} takes positive real values (representing, e.g., the fraction of the surface area of a colloidal particle covered by “patches” of certain types [8]) and \mathbf{u} takes negative real values (representing, e.g., the attractive interactions between patches). To ensure nonnegativity of \mathbf{W} and nonpositivity of \mathbf{u} , we apply a multiplicative update scheme, where \mathbf{W} and $-\mathbf{u}$ are multiplied by the ratio of the negative and positive parts of the corresponding gradient, $\nabla = \nabla^+ - \nabla^-$. We then let

$$W_{ia} \leftarrow W_{ia} \left(\frac{\nabla W_{ia}^-}{\nabla W_{ia}^+} \right), \quad (\text{S16})$$

$$-u_{ab} \leftarrow -u_{ab} \left(\frac{\nabla (-u)_{ab}^-}{\nabla (-u)_{ab}^+} \right). \quad (\text{S17})$$

This scheme is equivalent to gradient descent with a step size proportional to the ratio ∇^-/∇^+ . In the absence of any additional constraints, the update rules are thus

$$W_{ia} \leftarrow W_{ia} \left(\frac{(\epsilon \mathbf{W} \mathbf{u}^\top + \epsilon^\top \mathbf{W} \mathbf{u})_{ia}}{(\mathbf{W} \mathbf{u} \mathbf{W}^\top \mathbf{W} \mathbf{u}^\top + \mathbf{W} \mathbf{u}^\top \mathbf{W}^\top \mathbf{W} \mathbf{u})_{ia}} \right)^\gamma, \quad (\text{S18})$$

$$-u_{ab} \leftarrow -u_{ab} \left(\frac{(\mathbf{W}^\top \epsilon \mathbf{W})_{ab}}{(\mathbf{W}^\top \mathbf{W} \mathbf{u} \mathbf{W}^\top \mathbf{W})_{ab}} \right)^\gamma, \quad (\text{S19})$$

where we choose $\gamma = 1/4$ to ensure stable convergence. We can also include additional constraints, such as minimizing the variance of all monomer–monomer interactions or the variance of homotypic monomer–monomer interactions. These constraints can be easily implemented by adding the corresponding positive and negative parts of the constraints to the gradient, and then following the update scheme given above.

2. NMF with integer constraints

Imposing integer constraints on \mathbf{W} makes the NMF problem no longer convex in \mathbf{W} . Thus, in cases such as the heteropolymer design problem considered in the main text, where the molecular feature matrix must have integer entries (see also SI Sec. III A), optimizing \mathbf{W} becomes an NP-hard combinatorial optimization problem. For short polymer chains with $L_{\max} \lesssim 10$ and a prescribed monomer–monomer interaction matrix \mathbf{u} , it is feasible to find the globally optimal \mathbf{W} matrix by brute force. However, brute-force search is infeasible for designing long polymer chains. Instead, we follow an approach in which we sample \mathbf{W} matrices from a probability distribution, and then select candidate \mathbf{W} matrices from the tail of the reconstruction-error distribution. Suppose that every row of the \mathbf{W} matrix is drawn from a multinomial distribution $\vec{W}_i \sim \mathcal{M}_r(L_{\max}; \vec{p}_i)$ for $i = 1, \dots, N$, which gives the probability of any particular combination of counts for various feature types $a = 1, \dots, r$. The probability vector \vec{p}_i , which is normalized such that $\sum_{a=1}^r p_{ia} = 1$, parameterizes the multinomial distribution. In the heteropolymer design scenario, the number of categorical variables $r = \text{rank}(\epsilon_r)$ denotes the number of monomer types, L_{\max} is equal to the sum of the counts in \vec{W}_i , and p_{ia} represents the probability of adding a monomer of type a to chain i .

We are interested in finding an integer \mathbf{W} solution in which the reconstruction error is smaller than a prescribed threshold. If such \mathbf{W} matrices are rare, then we can carry out the search using a cross-entropy (CE) optimization approach [9]. This algorithm proceeds as follows:

1. Choose an initial parameter matrix \mathbf{p} , which contains all the probability vectors \vec{p}_i . Choose the total number of samples to be generated ($N_{\text{samples}} = 10000$) and the number of samples needed for parameter inference ($N_{\text{top}} = 10$). Let the initial iteration number be $t = 1$.
2. To generate a candidate solution pair (\mathbf{W}, \mathbf{u}) , sample each row $\vec{W}_1, \dots, \vec{W}_N \sim_{\text{iid}} \mathcal{M}_r(L_{\max}, \vec{p}_i)$. Then, given this candidate \mathbf{W} matrix, use gradient descent to optimize for a nonpositive \mathbf{u} matrix by iteratively applying the multiplicative update given in Eq. (S19) until convergence, defined as the point where the maximum difference between updates of any element of \mathbf{u} is less than 10^{-5} .
3. Repeat step 2 to generate N_{samples} samples and calculate the loss, Eq. (S15), for each sample.
4. Update $\mathbf{p}^{t+1} \leftarrow \mathbf{p}^t$ according to a maximum likelihood estimate. Specifically, determine the probability vectors \vec{p}_i^{t+1} by computing the normalized average frequencies of all monomer types observed in chain type i in the N_{top} candidate solutions with the smallest values of the loss.

5. Iterate steps 2, 3, and 4 until the maximum difference between updates of any element of the parameter matrix \mathbf{p} is less than 0.005 or the maximal number of iterations (chosen here to be 100) is exceeded. The (\mathbf{W}, \mathbf{u}) pair with the minimal loss is considered to be a solution if the reconstruction error is below the threshold, Eq. (S12).

We use uniform random initialization of the probability vectors to obtain all the design solutions presented in this paper. Because permutation of the rows of \mathbf{W} could potentially lead to degenerate solutions during the search, we sort the rows with respect to descending monomer frequencies for every candidate \mathbf{W} matrix. Furthermore, to make the optimization problem easier, we relax the constraint on the degree of polymerization by allowing the sequence length to be shorter than L_{\max} . To this end, we allow $\sum_{a=1}^r p_{ia} \leq 1$, which is realized in practice by adding a dummy column to the probability matrix \mathbf{p} . This enhanced-sampling method allows us to efficiently search for NMF solutions for arbitrary long polymer chains.

III. MULTICOMPONENT POLYMER MODEL AND SIMULATION METHODS

A. Multicomponent Flory–Huggins polymer model

We utilize the mean-field Flory–Huggins (FH) model to apply our theory to the design of Lennard–Jones heteropolymer solutions. The Helmholtz free-energy density, f ; chemical potential, $\vec{\mu} = \partial f / \partial \vec{\phi}$; osmotic pressure, P ; and Hessian matrix, $\partial^2 f / \partial \vec{\phi}^2 = \partial \vec{\mu}(\vec{\phi}) / \partial \vec{\phi}$, in the multicomponent Flory–Huggins model are

$$f = \sum_{i=1}^N \frac{\phi_i}{L_i} \log \phi_i + (1 - \phi_T) \log(1 - \phi_T) + \frac{1}{2} \sum_{i=1}^N \sum_{j=1}^N \epsilon_{ij} \phi_i \phi_j \quad (\text{S20a})$$

$$\mu_i = \frac{1}{L_i} \log \phi_i - \log(1 - \phi_T) - \left(1 - \frac{1}{L_i}\right) + \sum_{j=1}^N \epsilon_{ij} \phi_j \quad (\text{S20b})$$

$$P = -\log(1 - \phi_T) + \sum_{i=1}^N \frac{\phi_i}{L_i} - \phi_T + \frac{1}{2} \sum_{i=1}^N \sum_{j=1}^N \epsilon_{ij} \phi_i \phi_j \quad (\text{S20c})$$

$$\frac{\partial \mu_i}{\partial \phi_j} = \frac{\delta_{ij}}{L_i \phi_i} + \frac{1}{1 - \phi_T} + \epsilon_{ij}, \quad (\text{S20d})$$

respectively, where L_i is the degree of polymerization of polymeric species i . When applying our theory and design approach to multicomponent polymer solutions, we use these expressions in the convex relaxation, Eq. (S14).

When designing heteropolymers within this mean-field framework, we make a pairwise-additive assumption for the polymer–polymer interactions, ϵ . This means that the interaction matrix can be written as $\epsilon_{ij} = \sum_{a,b} W_{ia} u_{ab}^{L_i} W_{jb}$, where the molecular feature matrix, \mathbf{W} , is a count encoding of the occurrences of each monomer type, $a = 1, \dots, r$, within each polymer chain type, $i = 1, \dots, N$. This factorization of ϵ follows directly from the Flory–Huggins model, since the pairwise portion of the free-energy density, $(1/2) \sum_{i,j} \epsilon_{ij} \phi_i \phi_j$, represents the mean-field interaction between all pairs of monomers in a polymer solution [10]. More specifically, we can write this sum in the factorized form $(1/2) \sum_{i,j} \sum_{a,b} u_{ab} W_{ia} W_{jb} \phi_i \phi_j = (1/2) \sum_{a,b} u_{ab} \tilde{\phi}_a \tilde{\phi}_b$, where $\tilde{\phi}_a \equiv \sum_i W_{ia} \phi_i$ is the volume fraction occupied by monomers of type a . As we also emphasize in the main text, this pairwise-additive approximation for the polymer–polymer interactions is not an essential assumption of our theory, since we could directly determine the molecular features of heteropolymer interactions from simulations and then use these inferred features as a basis set for designing heteropolymer mixtures with prescribed polymer–polymer interactions. Such an approach could potentially capture sequence-patterning effects, which are explicitly ignored by the pairwise-additive assumption. (This topic will be the subject of future work.) Here we employ the pairwise-additive assumption because the meaning of the \mathbf{W} matrix is easy to understand in this case, thus providing a transparent proof-of-principle for our theory. We also show (see SI Sec. III E) that this approximation is surprisingly accurate for LJ heteropolymers under our simulation conditions.

B. Lennard–Jones heteropolymer model

1. Simulation model

We perform molecular simulations of heteropolymers in implicit solvent using a Lennard–Jones (LJ) polymer model using the LAMMPS simulation package [11]. Nonbonded monomers of types $a, b = 1, \dots, r$ interact via the LJ pair

potential [12],

$$U_{ab}^{\text{LJ}}(r) = 4w_{ab}^{\text{LJ}} [(d/r)^{12} - (d/r)^6] + U_{\text{cut},ab}, \quad (\text{S21})$$

where $w_{ab}^{\text{LJ}} < 0$ represents the interaction strength (i.e., well depth), d is the monomer diameter, and the cutoff distance is $3d$. The potential is shifted to zero at the cutoff distance by setting $U_{\text{cut},ab} = -4w_{ab}^{\text{LJ}}[(1/3)^{12} - (1/3)^6]$. Bonded monomers interact via finite-extensible nonlinear elastic (FENE) bonds [13], which comprise a nonlinear attractive term and a repulsive LJ term. For the FENE bonds, we use the parameters (100, 4, 1, 1), corresponding to the coefficient of the attractive term, the maximum length of the bond in units of d , the well depth for the LJ potential, and the diameter of the particle in units of d .

2. Constructing LJ interaction parameters and heteropolymer sequences

To perform simulation tests of our heteropolymer mixture designs, we need to construct LJ interaction matrices, $\{w_{ab}^{\text{LJ}}\}$, and polymer sequences using the optimal \mathbf{u}^{LJ} and \mathbf{W} matrices that we obtain via NMF (see Sec. IIB 2). We describe each of these steps in this section.

First, to convert between the mean-field monomer–monomer interaction coefficients, $\{u_{ab}^{\text{LJ}}\}$, and the well depths for the LJ interactions, $\{w_{ab}^{\text{LJ}}\}$, we perform a nonlinear mapping by matching the monomer–monomer second virial coefficients. Specifically, we approximate the repulsive part of the LJ potential using the hard-sphere potential, and then relate the attractive portion of the LJ second virial coefficient to u_{ab}^{LJ} ,

$$\frac{u_{ab}^{\text{LJ}}}{|\bar{u}^{\text{LJ}}|} = \frac{2\pi}{d^3} \int_d^{3d} dr r^2 \{1 - \exp[-U_{ab}^{\text{LJ}}(r)/k_{\text{B}}T]\}, \quad (\text{S22})$$

given a fixed temperature T . In practice, we work at a standard temperature, such that $k_{\text{B}}T = 1$ in our simulations. The user-defined scale factor, $|\bar{u}^{\text{LJ}}|$, controls the mean LJ interaction strengths used in the simulations; this scale factor must be introduced empirically (as opposed to being determined from the mean-field model) because the critical points of the mean-field FH model and the LJ heteropolymer simulations differ. In practice, we determine the LJ coefficients $\{w_{ab}^{\text{LJ}}\}$ from a designed monomer–monomer interaction matrix, \mathbf{u}^{LJ} , by choosing an appropriate value of $|\bar{u}^{\text{LJ}}|$ (determined from simulations of homomeric LJ heteropolymers with chain length L_{max}) and inverting Eq. (S22).

Second, to design the polymer sequences for polymer species $i = 1, \dots, N$, we utilize the count encodings in each row, \bar{W}_i , of the optimized molecular feature matrix. We aim to construct sequences that are minimally “blocky”, since the pairwise-additive assumption used in our heteropolymer design approach (see Sec. III A) does not consider sequence-patterning effects. We therefore aim to construct sequences in which the monomers of each type are homogeneously distributed throughout each polymer chain. Here we use a deterministic heuristic for interleaving different monomer types. To generate the sequence design for chain i , we first sort the monomer frequency counts $\{W_{ia}\}$ in descending order and associate the n th monomer of type a with the fractional number $n/(1 + W_{ia})$, where n goes from 1 to W_{ia} . We then read off the order of the monomer types in the sequence by going through the array of fractional numbers in ascending order.

Following these procedures, we obtain the LJ coefficients used for simulating the heteropolymer design shown in Fig. 3C in the main text,

$$\mathbf{w}^{\text{LJ}} = \begin{bmatrix} 0.520 & 0.863 & 0.380 \\ 0.863 & 0.345 & 0.238 \\ 0.380 & 0.238 & 0.788 \end{bmatrix}.$$

The corresponding sequences are shown in Fig. 3C of the main text.

C. Direct-coexistence simulations

1. Initialization of multiphase simulations

To prepare condensed phases for molecular dynamics simulations, we first perform constant-temperature-and-pressure (NPT) simulations for each individual target phase. We use $N_{\text{tot}} = 432$ chains in a cubic box with periodic boundary conditions, where chain types are assigned according to the target-phase composition. Performing NPT

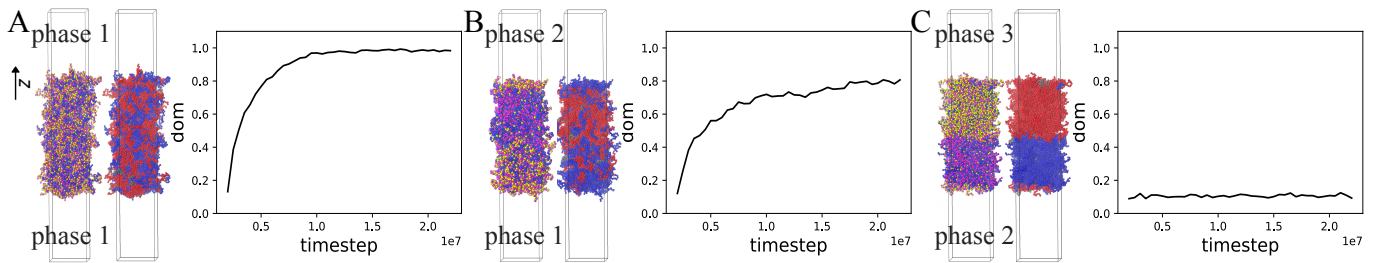


FIG. S1. **The degree of mixing as an indicator of equilibration.** For the example design solution shown in Fig. 3 in the main text, we compare the evolution of the degree of mixing (d.o.m.) between (A) an $\alpha = \beta$ control simulation and (B–C) two $\alpha \neq \beta$ direct-coexistence simulations. The left and right snapshots in each panel are colored according to the monomer types and the initial phase labels (either red or blue) at the end of the simulation trajectory. From **A**, we determine that the mixing timescale at this temperature and mean LJ interaction strength is approximately 10^7 timesteps ($5 \times 10^4 \tau$). The d.o.m. is significantly greater than zero in **B** because phases 1 and 2 share an enriched component. Interfacial effects, both at the α – β interface and at the condensed–dilute interfaces, also tend to increase the d.o.m. in both **B** and **C**.

simulations at zero pressure allows us to estimate the average equilibrium total number density in a condensed phase, ρ_{eq} . We then prepare the condensed phases for use in direct-coexistence simulations by deforming the simulation box. In this step, we maintain periodic boundary conditions in both the x and y directions while imposing hard wall constraints and open boundary conditions in the z direction. The final dimensions, consistent with the target density ρ_{eq} determined from the NPT simulations, are $l_z = 40d$ and $l_x = l_y = 20d$ for simulations of designs with $L_{\text{max}} = 20$, and $l_z = 40d$ and $l_x = l_y = 24.5d$ for simulations of designs with $L_{\text{max}} = 30$. Finally, the initial condition for a direct-coexistence simulation of a pair of condensed phases is constructed by stitching together two condensed phases and a dilute gas phase along the z axis of the simulation box. The region of the simulation box corresponding to the dilute phase is initialized with 6 chains of each type at a total number density of $\rho_{\text{dilute}} = 1.50 \times 10^{-3}$, 2.25×10^{-3} , or 1.50×10^{-3} for the designs shown in Fig. 3A, Fig. 5A, and Fig. 5C, respectively.

2. Production simulations

In our production runs, we perform constant-temperature-and-volume (NVT) direct-coexistence simulations. The overall dimensions of the simulation box, including α , β , and dilute phases, are $l = 20d \times 20d \times 120d$ for simulations of designs with $L_{\text{max}} = 20$, and $l = 24.5d \times 24.5d \times 120d$ for simulations of designs with $L_{\text{max}} = 30$. Each direct-coexistence simulation contains a total of $N_{\text{tot}} = 888$ chains for the four-component case and $N_{\text{tot}} = 900$ chains for the six-component cases. We perform NVT molecular dynamics simulations using the Nose–Hoover thermostat and a timestep of $5 \times 10^{-3} \tau$ (in LJ units).

To verify equilibration, we calculate the degree of mixing (d.o.m.) over the region of the simulation box that is occupied by condensed phases (Fig. S1). The d.o.m. is defined to be

$$\text{d.o.m.} \equiv 1 - \frac{1}{2} \int_{\phi_{\text{T}}(z) > 1/2} dz \frac{\left[p_{\text{init}}^{(\beta)}(z) - p_{\text{init}}^{(\alpha)}(z) \right]^2}{p_{\text{init}}^{(\alpha)}(z) + p_{\text{init}}^{(\beta)}(z)}, \quad (\text{S23})$$

where $p_{\text{init}}^{(\alpha)}(z)$ and $p_{\text{init}}^{(\beta)}(z)$ represent the probability of finding a chain that was initialized in the α or β condensed phase, respectively, at the position z along the simulation box. These probabilities are normalized such that $\int_{\phi_{\text{T}}(z) > 1/2} dz p_{\text{init}}^{(\alpha)} = 1$. If the chains completely mix, such that there is no correlation between the location of a particular chain and the condensed phase in which it was initially placed, then the degree of mixing tends to one. If the chains remain in their original phases, then the degree of mixing is close to zero. In situations where one or more species are shared between a pair of condensed phases, then the degree of mixing is expected to plateau at a value between zero and one. In practice, we use the degree of mixing to determine the timescale over which equilibration takes place in $\alpha = \beta$ control simulations (Fig. S1A). We also verify that the degree of mixing for $\alpha \neq \beta$ direct-coexistence simulations reaches a plateau value in the course of a simulation trajectory that is at least twice as long as the control-simulation mixing timescale (Fig. S1B–C).

D. Defining the heteropolymer design “fitness” metric

We compare alternative polymer designs by introducing an intuitive fitness metric based on the target order parameter profiles,

$$\text{fitness} \equiv \frac{\int_{\phi_{\text{T}}(z) > 1/2} dz \max_{\alpha} [q^{(\alpha)}(\vec{\phi}(z))]}{\int_{\phi_{\text{T}}(z) > 1/2} dz}, \quad (\text{S24})$$

where the order parameter is defined to be

$$q^{(\alpha)}(\vec{\phi}) \equiv \frac{\vec{\phi} \cdot \vec{\phi}^{(\alpha)}}{\|\vec{\phi}\| \|\vec{\phi}^{(\alpha)}\|}. \quad (\text{S25})$$

The fitness metric is equal to one if the bulk molecular concentrations in the condensed phases are precisely equal to the target molecular concentrations and the interfaces are perfectly sharp. However, in direct-coexistence simulations with α , β , and dilute phases, a valid design will lead to (at least) three finite-width interfaces. A lower bound on the fitness of a valid design can be estimated by assuming that the integrand in Eq. (S24) is zero in the interfacial regions and that there are three interfacial regions, each of which comprises at most 5% of the total region in which $\phi_{\text{T}} \geq 1/2$ (based on the typical interfacial width in the control simulations shown in Fig. S1A). In this way, we estimate that a valid design should have a fitness score of at least 0.85. We use this value as the threshold for determining whether a heteropolymer design is a success or a failure in Figs. 3 and 5 in the main text. We note that this heuristic fitness metric might not work as well as the number of components increases, since the order parameter is based on a Euclidean distance, and it generally becomes harder to distinguish points in high-dimensional spaces in this way due to the curse of dimensionality.

The equilibrated concentration and order-parameter profiles of the alternative designs for the example four-component design problem (see Fig. 3 in the main text) are shown in Fig. S2.

E. Computing effective polymer–polymer interactions in dilute and condensed phases

1. Effective polymer–polymer interactions in the dilute limit

Polymer–polymer interactions in the dilute limit can be quantified by second virial coefficients [14],

$$B_{ij}^{\text{sim}} = 2\pi \int_0^{\infty} dr r^2 \{1 - \exp[-w_{ij}(r)/k_{\text{B}}T]\}, \quad (\text{S26})$$

where $w_{ij}(r)$ is the simulated potential of mean force (PMF) between the centers of mass of two polymers of types i and j . In practice, we compute $w_{ij}(r)$ using adaptive biasing force (ABF) simulations [15] implemented via the COLVARS package [16] in LAMMPS [11]. We run constant-temperature-and-volume (NVT) simulations with two chains initialized in a $20d \times 20d \times 20d$ simulation box with shrink-wrapped boundary conditions. Force statistics are stored in bins of width $0.25d$. The biasing force is applied once 1000 samples are collected in each bin, after which a final production run is performed for 10^8 steps with a timestep of 0.005τ (in LJ units). The second virial coefficient is then obtained by integrating the PMF using Eq. (S26). In Fig. 4a in the main text, five independent ABF simulations are performed for each B_{ij} calculation to determine the statistical errors, shown as error bars in Fig. 4A in the main text.

We then compare the second virial coefficients computed via simulation to those predicted by the Flory–Huggins model,

$$B_{ij}^{\text{FH}} = \frac{d^3 L_i L_j (1 + \epsilon_{ij}/k_{\text{B}}T)}{2}. \quad (\text{S27})$$

This comparison is shown in Fig. 4A in the main text.

2. Effective polymer–polymer interactions in condensed phases: Excess chemical potential differences

We extract the excess chemical potential differences, $\Delta_{\alpha\beta}\mu_{\text{ex},i} \equiv \mu_{\text{ex},i}^{(\beta)} - \mu_{\text{ex},i}^{(\alpha)}$, from the equilibrium compositions, determined from direct-coexistence simulations, of simulated α and β bulk phases via [17]

$$\Delta_{\alpha\beta}\mu_{\text{ex},i}^{\text{sim}} = k_{\text{B}}T \log \left(\frac{\langle \phi_i^{(\alpha)} \rangle}{\langle \phi_i^{(\beta)} \rangle} \right). \quad (\text{S28})$$

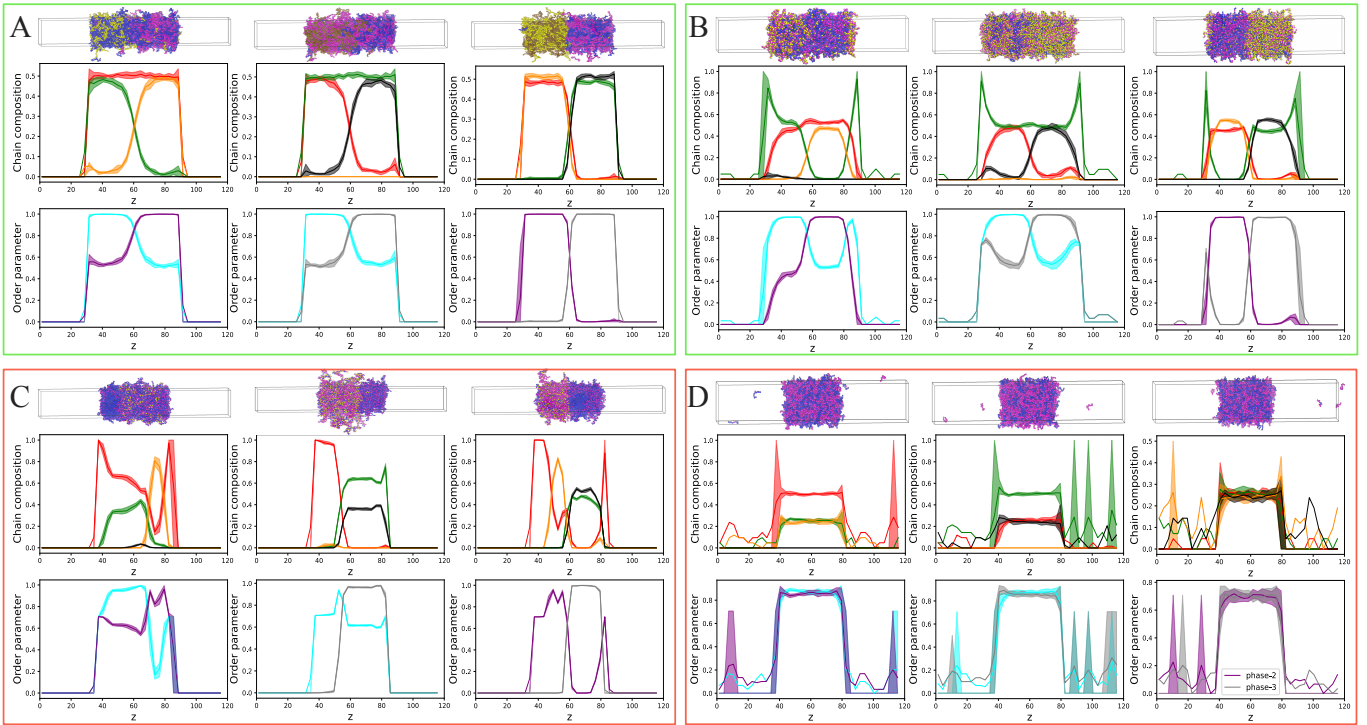


FIG. S2. **Simulation results for alternative design strategies.** Simulation results are shown for the alternative LJ heteropolymer designs summarized in Fig. 3b of the main text. Data are presented as in Fig. 3a of the main text. (A) A full-rank $r = 4$ design. The interaction matrix is obtained by minimizing the variance of the independent entries of ϵ , as in Ref. [2]. (B) The $r = 3$ design shown in Fig. 3a in the main text. (C) A design obtained by running the NMF solver on the interaction matrix used in **A**, but enforcing $r = 3$ monomer types. (D) A design obtained by running the NMF solver on the optimized $r = 3$ interaction matrix used in **B**, but enforcing $r = 2$ monomer types. The green and red outlines around each panel indicate whether the design is determined to be a success or a failure, respectively, according to the fitness metric, Eq. (S24).

We then compare these calculations with the Flory–Huggins prediction,

$$\Delta_{\alpha\beta}\mu_{\text{ex},i}^{\text{FH}} = -k_{\text{B}}T \log\left[\frac{1 - \phi_{\text{T}}^{(\beta)}}{1 - \phi_{\text{T}}^{(\alpha)}}\right] + \sum_j \epsilon_{ij}(\phi_j^{(\beta)} - \phi_j^{(\alpha)}). \quad (\text{S29})$$

This comparison is shown in Fig. 4B in the main text.

3. Effective polymer–polymer interactions in condensed phases: Radial distribution functions and structure factors

For each condensed phase, we run an NPT simulation at zero pressure to compute the radial distribution function (RDF) with respect to the center of mass distance between polymers of various species (Fig. S3A). The RDF between chain types i and j is denoted $g_{ij}(r)$. Note that this calculation can only be performed with sufficient statistical accuracy for chain types that are enriched in a particular condensed phase. From the RDFs, we measure the well depths of the interactions, $\min_r -\log g_{ij}(r)$, which strongly correlate with the predicted pairwise interactions, ϵ_{ij} (Fig. S3B). This correspondence provides additional support for our conclusion that the mean-field approximations hold better in the condensed phases than in the dilute phase.

The mean-field interactions can also be related to the RDFs using linear response theory [14]. Specifically, the partial structure factor is related to the Fourier transform of the pair correlation function, $\hat{h} \equiv \hat{g} - 1$, via

$$S_{ij}(\vec{k}) = x_i\delta_{ij} + x_i x_j \rho \hat{h}_{ij}(\vec{k}), \quad (\text{S30})$$

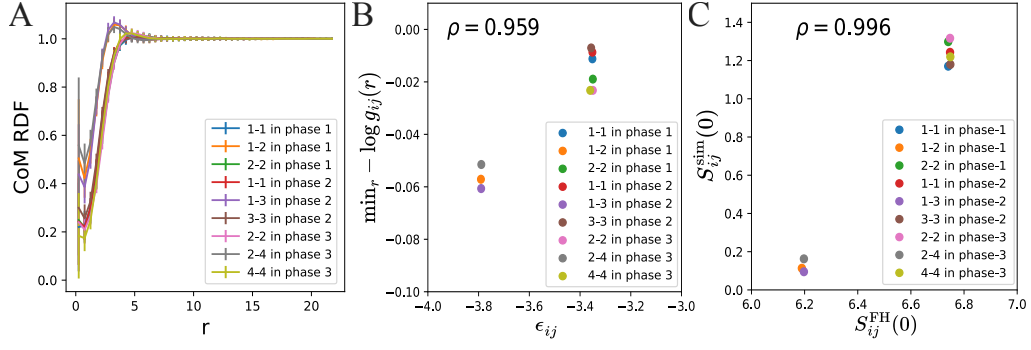


FIG. S3. **Effective polymer–polymer interactions determined from radial distribution functions (RDFs).** (A) RDFs, $g_{ij}(r)$, between the centers of mass (CoMs) of chains in the condensed phases. Only enriched chain types are shown for each condensed phase. (B) Correlations between the effective well depths inferred from the RDFs (see text) and the pairwise interactions, ϵ_{ij} . The legend indicates pairs of chain types. (C) Correlations between the zero-mode partial structure factors, $S_{ij}^{\text{sim}}(0)$, determined from the RDFs and the mean-field interactions in the Flory–Huggins model. In **B** and **C**, the Pearson correlation coefficient, ρ , is indicated.

where $x_i = \phi_i/\phi_T$ is the chain composition in a condensed phase, $\rho = N_{\text{tot}}/V$ is the total number density in the condensed phase, and V is the simulated volume of the condensed phase. It follows that

$$\begin{aligned} \lim_{|\vec{k}| \rightarrow 0} S_{ij}(\vec{k}) &= x_i \delta_{ij} + 2x_i x_j \rho \int_0^\infty dr r h(r) \times \lim_{|\vec{k}| \rightarrow 0} \frac{\sin(2\pi r |\vec{k}|)}{|\vec{k}|} \\ &= x_i \delta_{ij} + 4\pi x_i x_j \rho \int_0^\infty dr r^2 h(r). \end{aligned} \quad (\text{S31})$$

Finally, from linear response theory [14], we find

$$S_{ij}(0) = V^{-1} \frac{\partial \langle N_i \rangle}{\partial \beta \mu_j} = k_B T \left(\frac{\partial \mu_j}{\partial \rho_i} \right)^{-1} = k_B T \left(L_i \frac{\partial \mu_j}{\partial \phi_i} \right)^{-1}. \quad (\text{S32})$$

We calculate the zero mode for number density fluctuations, $S_{ij}(0)$, via the mean-field expression, Eq. (S20)d, and the simulated single-phase RDFs, Eq. (S31), and find that the results are highly correlated (Fig. S3C). This finding also supports our conclusion that the mean-field approximations hold well in the condensed phases.

We compute the overlap parameter, P [10], from these single-phase simulations by estimating the median number of distinct neighboring chains with which every chain in a condensed phase interacts. A chain is considered to be an interacting neighbor if there is at least one inter-chain pair of monomers that are within the cutoff distance, $3d$, of the monomer–monomer LJ potential.

IV. DESIGN AND SIMULATION DATA FOR 6-COMPONENT HETEROPOLYMER DESIGNS

In this section, we present the optimization results and resulting simulation data for the problems considered in Figs. 5A and 5C in the main text. The results of convex optimization for both problems are shown in Fig. S4 using the same format as in Fig. 3A of the main text. For the condensate design problem shown in Fig. 5A, we select the optimal solution using the parameters $\lambda_{\text{min}} = 0.5k_B T$ and $L_{\text{max}} = 20$. For the condensate design problem shown in Fig. 5C, we select the optimal solution using the parameters $\lambda_{\text{min}} = 0.075k_B T$ and $L_{\text{max}} = 30$.

The LJ coefficients used for simulating the heteropolymer design shown in Fig. 5A in the main text are

$$\mathbf{w}^{\text{LJ}} = \begin{bmatrix} 0.630 & 0.559 & 0.430 & 0.264 \\ 0.559 & 0.582 & 0.374 & 0.877 \\ 0.430 & 0.374 & 0.516 & 0.361 \\ 0.264 & 0.877 & 0.361 & 0.663 \end{bmatrix}.$$

The LJ coefficients used for simulating the heteropolymer design shown in Fig. 5C in the main text are

$$\mathbf{w}^{\text{LJ}} = \begin{bmatrix} 0.135 & 0.701 & 0.482 & 0.457 \\ 0.701 & 0.483 & 0.271 & 0.375 \\ 0.482 & 0.271 & 0.951 & 0.525 \\ 0.457 & 0.375 & 0.525 & 0.982 \end{bmatrix}.$$

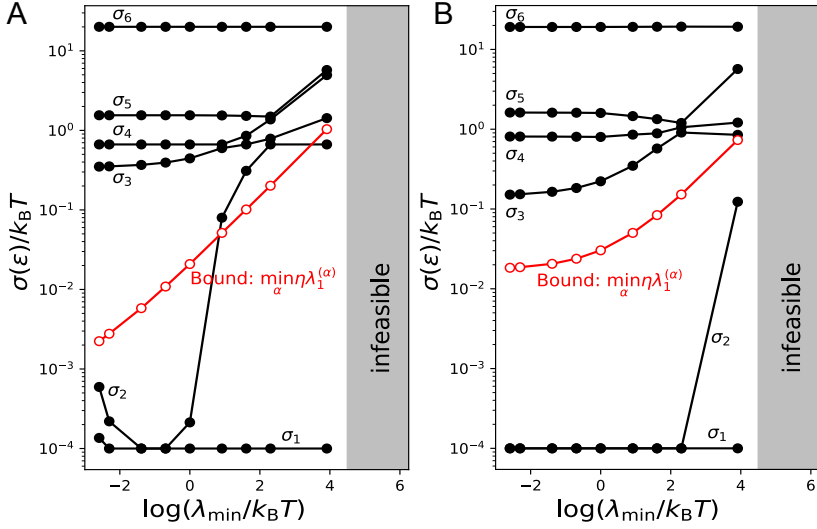


FIG. S4. **Convex optimization results for example six-component condensate design problems.** Data are shown as in Fig. 3A of the main text. (A) Convex optimization results for the condensate design problem shown in Fig. 5A in the main text. (B) Convex optimization results for the condensate design problem shown in Fig. 5C in the main text.

The corresponding simulation data for these designs, along with the optimized sequences shown in Figs. 5A and 5C in the main text, are shown in Fig. S5.

[1] C. Eckart and G. Young, *Psychometrika* **1**, 211–218 (1936).
 [2] F. Chen and W. M. Jacobs, *J. Chem. Phys.* **158**, 214118 (2023).
 [3] S. P. Boyd and L. Vandenberghe, *Convex optimization* (Cambridge University Press, 2004).
 [4] S. Diamond and S. Boyd, *J. Mach. Learn. Res.* **17**, 2909 (2016).
 [5] B. O’Donoghue, E. Chu, N. Parikh, and S. Boyd, *J. Optimiz. Theory App.* **169**, 1042 (2016).
 [6] B. Recht, M. Fazel, and P. A. Parrilo, *SIAM Review* **52**, 471–501 (2010).
 [7] Z. Yang and E. Oja, *Pattern Recognition* **45**, 1500 (2012).
 [8] S. C. Glotzer and M. J. Solomon, *Nat. Mater.* **6**, 557 (2007).
 [9] P.-T. De Boer, D. P. Kroese, S. Mannor, and R. Y. Rubinstein, *Ann. Oper. Res.* **134**, 19 (2005).
 [10] R. H. Colby and M. Rubinstein, *Polymer physics* (Oxford University Press, 2003).
 [11] S. Plimpton, *J. Comput. Phys.* **117**, 1 (1995).
 [12] J. E. Lennard-Jones, *Proc. Royal Soc. A* **106**, 463–477 (1924).
 [13] K. Kremer and G. S. Grest, *J. Chem. Phys.* **92**, 5057–5086 (1990).
 [14] J.-P. Hansen and I. R. McDonald, *Theory of simple liquids: With applications to soft matter* (Academic Press, 2013).
 [15] E. Darve, D. Rodríguez-Gómez, and A. Pohorille, *J. Chem. Phys.* **128** (2008).
 [16] J. Hémin, G. Fiorin, C. Chipot, and M. L. Klein, *Journal of Chemical Theory and Computation* **6**, 35–47 (2009).
 [17] W. M. Jacobs, *J. Chem. Theory Comput.* **19**, 3429 (2023).

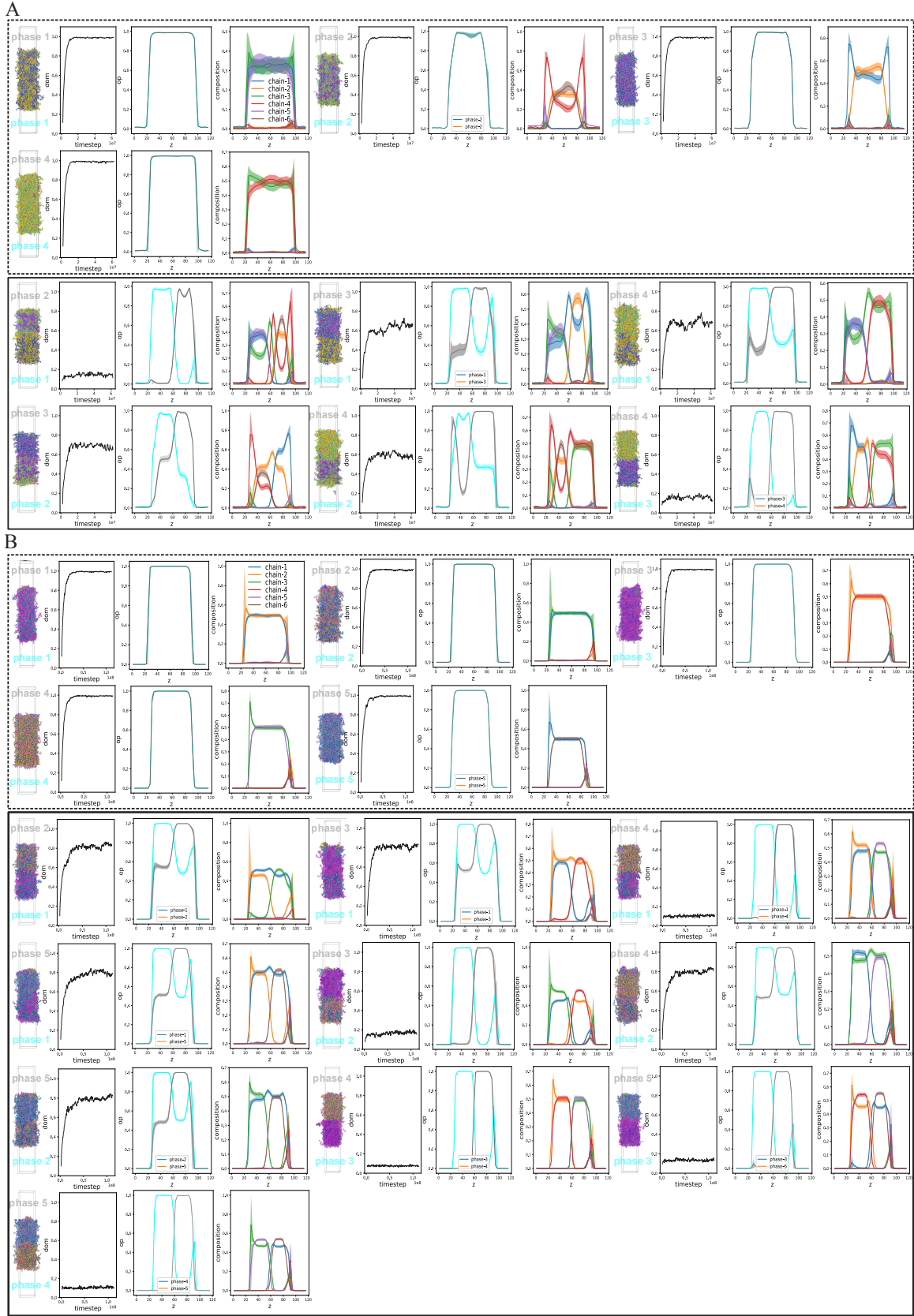


FIG. S5. Molecular simulation results for optimized LJ heteropolymer solutions to example six-component condensate design problems. Simulation results of all pairs of coexisting phases are shown for (A) the condensate design problem presented in Fig. 5A of the main text and (B) Fig. 5C of the main text. Results in dashed boxes correspond to control simulations, for which $\alpha = \beta$. Results in solid boxes correspond to direct-coexistence simulations of immiscible phases, for which $\alpha \neq \beta$.